Microporous and Mesoporous Materials 413 (2026) 114277

Contents lists available at ScienceDirect

Microporous and Mesoporous Materials

journal homepage: www.elsevier.com/locate/micromeso

Determining role of surface chemistry and textural architecture in methylene blue adsorption and hydrogen storage in sepiolite

Berna Koçer Kizilduman

Balikesir University Faculty of Arts and Sciences Department of Chemistry, Balikesir, 10145, Turkey

ARTICLE INFO

Keywords:
Sepiolite
Modification
Methylene blue
Hydrogen storage
Adsorption mechanism

ABSTRACT

In this study, natural sepiolite and APTES-functionalized sepiolite were investigated as multifunctional clay-based materials for aqueous-phase methylene blue (MB) removal and gas-phase hydrogen storage. The effects of surface chemistry and pore architecture on adsorption performance were systematically evaluated through FTIR, XRD, BET, SEM/EDX, TGA/DTG, and zeta potential analyses. The results showed that APTES functionalization preserved the fibrous structure of sepiolite while reducing micropore accessibility and specific surface area. Electrokinetic measurements revealed a shift of the isoelectric point toward more acidic values and the predominance of negative surface charge over a wide pH range, enhancing electrostatic interactions with cationic MB molecules. Consequently, the modified sample exhibited improved liquid-phase adsorption performance. Adsorption capacity and adsorption rate increased with increasing stirring speed, initial dye concentration, pH, and temperature, whereas adsorption was limited under acidic conditions and low stirring rates. Kinetic modeling indicated that the adsorption process was best described by the pseudo-second-order model and followed a multi-step mechanism involving film diffusion, intraparticle diffusion, and surface interactions. Hydrogen storage experiments demonstrated that adsorption was predominantly governed by physisorption and strongly influenced by microporous structure. Natural sepiolite exhibited higher hydrogen uptake than the modified sample due to its greater micropore accessibility. Overall, liquid-phase adsorption was controlled primarily by surface chemistry and electrokinetic properties, whereas gas-phase hydrogen storage was dictated by pore architecture. These findings provide insights into the development of multifunctional clay-based materials for environmental remediation and hydrogen-storage applications.

1. Introduction

With the rapid expansion of industrial activities, contamination of water resources by persistent organic pollutants has become a major environmental concern. In particular, synthetic dyes discharged from textile, paint, and chemical industries exhibit high chemical stability and resistance to biodegradation, allowing them to persist in aquatic environments for extended periods [1,2]. These dyes reduce light penetration in aquatic systems, suppress photosynthetic activity, and pose ecological and human health risks due to their toxic effects [3]. Methylene blue (MB), owing to its cationic structure and high solubility, is widely employed as a model pollutant, and its effective removal is of considerable importance for environmental sustainability. Among various dye removal techniques, adsorption stands out due to its high efficiency, operational simplicity, and economic feasibility [4]. The efficiency of the adsorption process is strongly governed by the surface chemistry, pore structure, and active functional groups of the adsorbent. In this context, clay minerals represent promising adsorbents because of their natural abundance, low cost, and chemical stability.

Sepiolite is a fibrous magnesium silicate clay mineral with a 2:1 trioctahedral structure. Its channel–type nanoporous framework and surface silanol (Si–OH) groups provide a high specific surface area and reactive surface characteristics [5]. These structural features render sepiolite particularly suitable for the adsorption of organic molecules. Furthermore, its thermal behavior and structural water loss can modify pore architecture and surface properties, thereby influencing adsorption performance [6]. Various surface modification strategies have been employed to enhance and tailor the adsorption performance of sepiolite. Amino–functionalization introduces additional active sites onto the surface and can modify adsorption performance toward organic pollutants through electrostatic interactions and hydrogen bonding mechanisms. However, adsorption is generally a multi–step process involving film diffusion, surface adsorption, and intraparticle diffusion. Therefore, kinetic modeling plays a critical role in identifying the rate–controlling

E-mail address: bernakocer@balikesir.edu.tr.

https://doi.org/10.1016/j.micromeso.2026.114277
Received 11 March 2026; Received in revised form 2 June 2026; Accepted 9 June 2026
Available online 13 June 2026

steps. The pseudo–first–order and pseudo–second–order models are widely employed to describe adsorption kinetics, while the Weber–Morris model is used to evaluate the contribution of intraparticle diffusion [7,8].

Recent studies have demonstrated that clay minerals possess potential not only for liquid–phase pollutant removal but also for gas–phase applications [9–13]. Hydrogen is considered a clean energy carrier due to its high energy density and carbon–free combustion [14]. Nevertheless, the safe and efficient storage of hydrogen remains a significant engineering challenge. Physical adsorption–based storage systems using porous materials offer an alternative approach in this regard. Hydrogen adsorption in clay minerals has been reported to depend strongly on surface area, pore structure, pressure, and temperature conditions [10]. Owing to its fibrous and channel–like structure, sepiolite has been reported to exhibit higher hydrogen adsorption capacity than layered clay minerals [12]. However, existing studies predominantly focus on gas–-phase adsorption, and a combined evaluation of liquid–phase adsorption performance and hydrogen storage behavior within a single framework remains largely unexplored. The development of multifunctional adsorbents capable of simultaneously addressing environmental remediation and energy-storage challenges has recently attracted increasing attention. In this context, clay-based materials are particularly attractive because their surface chemistry can be tailored for aqueous-phase pollutant removal, while their porous architecture may also provide adsorption sites for hydrogen storage. However, studies integrating these two functionalities within a single sepiolite-based material platform remain extremely limited. Although sepiolite has been extensively investigated either as an adsorbent for aqueous contaminants or as a porous material for hydrogen storage, these applications have almost exclusively been studied independently. Consequently, the relationship between surface functionalization, adsorption mechanisms, and structure–property interactions across liquid and gas phases remains poorly understood. Establishing such a comparative understanding is essential for the rational design of multifunctional adsorbents capable of serving both environmental and energy-related applications.

Accordingly, this study aims to comparatively investigate the liquid-phase and gas-phase adsorption behavior of natural and amino-functionalized sepiolite and to elucidate how surface modification influences adsorption kinetics, diffusion mechanisms, and structure–function relationships. The materials were comprehensively characterized using Brunauer–Emmett–Teller (BET) surface area analysis, Fourier-transform infrared (FTIR) spectroscopy, X-ray diffraction (XRD), thermogravimetric and derivative thermogravimetric (TGA/DTG) analyses, and scanning electron microscopy coupled with energy-dispersive X-ray spectroscopy (SEM/EDX) techniques. The electrokinetic properties of the modified sepiolite were determined as a function of pH using a Malvern Nano Zetasizer S, and the effect of surface charge behavior on adsorption processes was evaluated. MB adsorption experiments were conducted exclusively on amino–functionalized sepiolite, whereas hydrogen storage behavior was assessed for both natural and amino–functionalized sepiolite samples. To elucidate the kinetic and mechanistic aspects of the adsorption processes, both liquid–phase MB adsorption and gas–phase hydrogen storage data were analyzed using pseudo–first–order and pseudo–second–order kinetic models. In addition, the Weber–Morris diffusion model was applied to determine the role of mass transfer and intraparticle diffusion in both adsorption systems. Hydrogen adsorption measurements were performed over a wide pressure range at 77 and 298 K using a Hiden IMI PSI high–pressure gas adsorption system.

To the best of our knowledge, this is the first study to comparatively investigate aqueous-phase methylene blue adsorption and high-pressure hydrogen storage performance of sepiolite-based materials within a unified kinetic, diffusion, and structure–function analysis framework. By correlating electrokinetic behavior, surface chemistry, and pore architecture with adsorption performance across different phases, the present work establishes a comprehensive understanding of the mechanisms governing multifunctional adsorption systems. Beyond evaluating adsorption performance alone, this study highlights the feasibility of utilizing a single clay-based material platform for both pollutant removal and hydrogen-storage applications, thereby contributing to the development of next-generation multifunctional adsorbents.

2. Materials and methods

2.1. Materials

Sepiolite samples were obtained from Aktaş Lületaşı Co. (Eskişehir, Turkey). They were purified before being used in experiments [15]. A suspension containing 10 g/L sepiolite was mechanically stirred for 24 h and then allowed to settle for 5 min. The resulting suspension was subsequently filtered through filter paper. The samples collected with filter paper were dried at 105 °C for 24 h, ground in a Fritsch Premium–Line Pulverisette 7 ball mill and sieved with a 50 μm sieve using Retsch AS 200 vibrating siever. The organo–modifier, (3–aminopropyl) triethoxysilane (APTES), toluene, methanol and acetone were purchased from Sigma–Aldrich Company. MB with a molecular weight of 373.9 g/mol was obtained from Carlo Erba. Hydrochloric acid (HCl) and sodium hydroxide (NaOH) were provided from Merck. All chemicals were of analytical grade and used as received without further purification.

2.2. Methods

2.2.1. Surface modification of sepiolite with APTES

The modification process was carried out in 100 mL of toluene solution. 5 mL of APTES was added to the toluene solution and the temperature was fixed at 80 °C. Then, 5 g of sepiolite was added to this solution, magnetically stirred under reflux for 24 h. The reaction product was filtered with filter paper and washed with toluene, then with methanol and acetone, and the modified sepiolite was dried at 80 °C for 24 h [16].

2.2.2. Adsorption kinetics experiments

The adsorption kinetics experiments of MB on the modified sepiolite surface were investigated at different stirring speeds, initial dye concentrations, pHs and temperatures. All MB solutions were prepared with distilled water. The pH of the solutions was adjusted with HCl and NaOH solutions using the Orion 920A pH meter equipped with a combined electrode. Adsorption experiments were conducted at different stirring speeds (250, 500 and 750 rpm), initial dye concentrations (1×10^{-4}, 5×10^{-5}, 1×10^{-5} mol/L), pHs (3, 5, 7 and 9) and temperatures (30, 40, 50 and 60 °C). In the experiments, 1 g of modified sepiolite was added to 1 L of MB solution. Preliminary experiments indicated that adsorption equilibrium was reached within approximately 300 min. Therefore, all experiments were conducted for 300 min under continuous stirring using a temperature-controlled magnetic stirrer. Samples of 1 mL were taken at certain time intervals within 300 min period. The sample solutions were centrifuged at 5000 rpm for 15 min. To calculate the amount of MB adsorbed on the modified sepiolite, the absorbance values of the samples taken from the solution phase of each series of experiments were determined using PerkinElmer Lambda 25 UV–Vis spectrophotometer at a wavelength of 663 nm, where MB showed maximum absorbance. A calibration curve was established using standard MB solutions measured at the same wavelength. The amount of MB adsorbed onto the modified sepiolite at any time (q_t) was calculated from the difference between the initial and residual solution concentrations. The amount of dye adsorbed on modified sepiolite at any time, t, was calculated from the concentrations in solutions before and after adsorption. The mass balance (q_e) (mol/g) of the amount of MB adsorbed on the modified sepiolite was calculated as follows.

$$q_e = (C_0 - C_e)\frac{V}{m} \quad (1)$$

where C_0 and C_e are the initial and equilibrium concentrations of MB in solution (mol/L), respectively; V is the solution volume (L), and m is the mass of modified sepiolite (g) [17].

2.2.3. Hydrogen storage

The hydrogen storage behavior of sepiolite and APTES–functionalized sepiolite samples was investigated using a Hiden IMI PSI high–pressure gas storage system. Prior to the measurements, the samples were degassed under vacuum at 105 °C for 4 h in order to remove moisture and volatile species adsorbed on the surface. Subsequently, the hydrogen storage capacity was measured over a range of pressures under both ambient and cryogenic temperature conditions [18].

2.3. Characterization

FTIR–ATR analyses of the samples were performed with PerkinElmer Spectrum 100 spectrophotometer in the transmittance mode in the wavenumber range of 4000–650 cm^{-1}. XRD analysis was performed using a Rigaku MiniFlex 600 diffractometer operated at 40 kV and 15 mA, with a scan range of 5–90° and a step width of 0.01°. TGA/DTG analysis were performed using a PerkinElmer Diamond DTA/TG simultaneous thermal analyzer at a heating rate of 20 °C/min from 30 to 1200 °C under a nitrogen atmosphere. Prior to microscopic examination, the samples were coated with Au–Pd for 60 s under a current of 20 mA to improve conductivity. Surface morphology was investigated using a ZEISS Sigma 300 field-emission scanning electron microscope (FESEM). Elemental compositions were determined using a ZEISS EVO LS 10 scanning electron microscope equipped with a Bruker energy-dispersive X-ray spectroscopy (EDX) detector. BET surface area measurements of samples were performed using Quantachrome Nova 2200e series BET surface area analyzer in liquid nitrogen (77 K) using N_2 gas as adsorbate. Before performing BET surface area measurements, sepiolite samples were degassed at 105 °C for 4 h. Zeta potential measurements were performed with the Malvern Zetasizer Nano–S instrument. Suspensions containing 0.05 g of modified sepiolite in 10 mL of distilled water were conditioned for 3 h at different pH values prior to measurement. The suspension pH was adjusted with dilute HCl and NaOH solution. Measurements were made after the suspension was rested for 5 min to allow the coarse particles to settle to the bottom. At least 3 repeated measurements were taken with the prepared suspensions [19].

3. Results and discussions

3.1. Characterization

To elucidate the structure–surface–function relationships of pristine sepiolite, amino–functionalized sepiolite, and MB–adsorbed modified sepiolite, a comprehensive characterization study involving FTIR–ATR, TGA/DTG, SEM/EDX, and N_2 adsorption–desorption (BET) analyses was conducted. The results obtained from these techniques are discussed in detail below.

3.1.1. FTIR–ATR analysis

The FTIR–ATR spectra of pristine and APTES–functionalized sepiolite (Fig. 1) provide direct spectroscopic evidence of surface modification while simultaneously confirming preservation of the silicate framework. The characteristic structural bands of sepiolite remain clearly preserved after modification, indicating that the grafting process does not disrupt the fundamental tetrahedral–octahedral structure of the mineral. In the high–wavenumber region, the band at 3686 cm^{-1} assigned to Mg_3OH stretching and the band at 3624 cm^{-1} corresponding to structurally bound water are retained, suggesting that the internal lattice hydroxyl groups remain largely unaffected [20]. The absorption features at 3564 cm^{-1} and 1659 cm^{-1} associated with zeolitic water confined within the channels are also preserved, confirming the structural integrity of the fibrous channel system. The most pronounced spectral changes occur in the organic vibration and silicate fingerprint regions. After modification, a new band at approximately 2935 cm^{-1} appears and is assigned to C–H stretching of the propyl chain of APTES [21,22]. In addition, the band at 1473 cm^{-1} corresponding to C–N stretching confirms the successful incorporation of amine functionalities onto the sepiolite surface. These bands are absent in pristine sepiolite and therefore provide strong spectroscopic evidence for successful

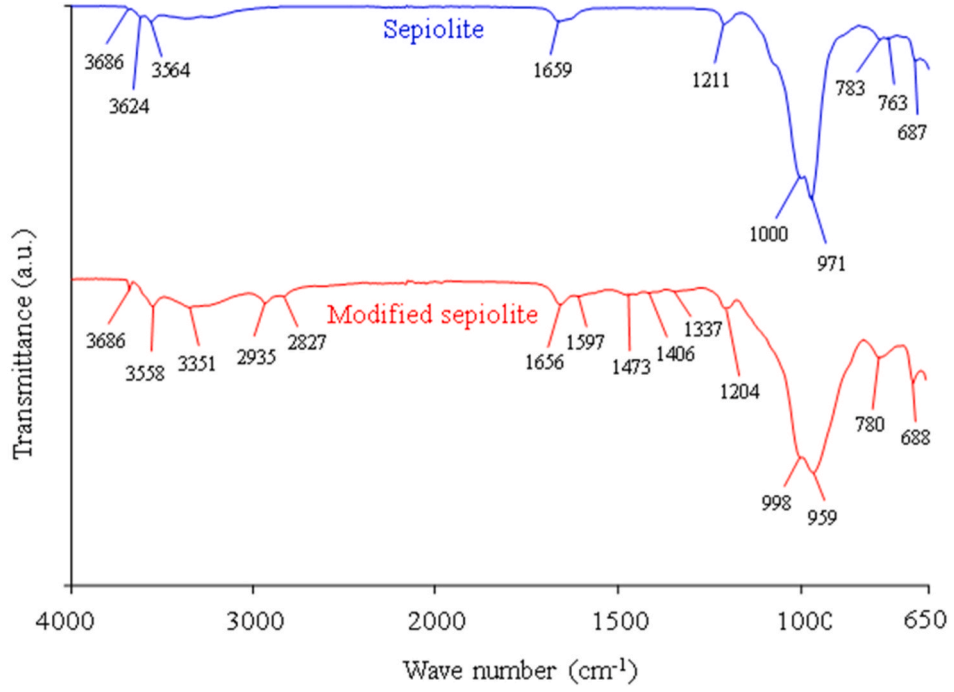

Fig. 1. FTIR–ATR spectra of sepiolite and APTES–fuctionalized sepiolite confirming surface functionalization.

organosilane grafting. Systematic but subtle shifts observed in the Si–O related bands further support chemical interaction between the silane modifier and surface silanol groups. The Si–O vibration at 971 cm^{-1} shifts to 959 cm^{-1}, while the Si–O–Si stretching band at 1000 cm^{-1} shifts slightly to 998 cm^{-1} after modification. Similar band displacements have been reported for silane–treated clay minerals and are commonly attributed to the formation of new Si–O–Si linkages through condensation reactions between surface Si–OH groups and hydrolyzed ethoxy groups of silane coupling agents [23,24]. These spectroscopic features are consistent with the surface grafting mechanism illustrated in Fig. 2, where APTES undergoes hydrolysis followed by condensation with surface silanol (Si–OH) groups of sepiolite under reflux conditions, forming covalently anchored Si–O–Si bonds and surface–exposed amine ($–NH_2$) functionalities. This mechanism rationalizes both the emergence of organosilane–related vibrational bands and the slight shifts observed in the silicate framework region. Importantly, the absence of significant band broadening or collapse within the silicate lattice region indicates that grafting occurs predominantly at accessible surface hydroxyl sites without structural degradation. This observation is consistent with the formation of a surface–bound organosilane layer rather than intercalation or framework substitution.

From a mechanistic standpoint, the FTIR–ATR data indicate that modification proceeds via hydrolysis of ethoxy groups followed by condensation with surface silanol groups, yielding covalently anchored propylamine chains. The introduction of amine functionalities modifies the surface chemical environment and charge distribution, in agreement with the zeta potential behavior discussed in Section 3.2. Furthermore, preservation of the silicate backbone together with the emergence of organic functional groups has direct implications for adsorption behavior. Structural integrity maintains the nanochannel network required for hydrogen diffusion, whereas grafted amine groups introduce additional interaction sites for cationic dye molecules and may alter electrostatic interactions and diffusion pathways. Accordingly, the FTIR results provide the chemical basis for interpreting the distinct behaviors observed in MB adsorption and hydrogen storage performance.

3.1.2. XRD analysis

The XRD patterns of pristine sepiolite and APTES-functionalized sepiolite are presented in Fig. 3. The diffraction pattern of pristine sepiolite exhibits the characteristic reflections of sepiolite at 2θ values of approximately 7.32°, 11.81°, 13.34°, 19.67°, 20.55°, 23.69°, 26.58°, 27.90°, and 34.84°, which are in good agreement with the crystallographic data reported for sepiolite (COD 9016669). Qualitative phase analysis confirmed that sepiolite is the only detectable crystalline phase in the investigated sample, and no reflections attributable to associated minerals such as quartz, calcite, dolomite, or feldspar were identified within the detection limits of the measurement. This result indicates the high mineralogical purity of the raw sepiolite used in the present study. The absence of detectable impurity phases is consistent with the supplier specifications and confirms the suitability of the material for investigating structure–property relationships without interference from secondary mineral phases. Following APTES functionalization, the characteristic diffraction peaks remain clearly visible at nearly identical diffraction angles (7.37°, 11.83°, 13.30°, 19.70°, 20.58°, 23.71°, 26.62°, 27.95°, and 34.77°), indicating that the crystalline framework of sepiolite is preserved during the silanization process. The absence of new diffraction peaks after modification further suggests that the grafted organosilane species are predominantly distributed on the external surface rather than forming a separate crystalline phase. Similar behavior has frequently been reported for silane-functionalized clay minerals, where surface grafting alters surface chemistry without disrupting the underlying crystal structure. The slight decrease in relative peak intensities observed after functionalization may be associated with the presence of an amorphous organosilane layer partially covering the crystal surface. These changes may be attributed to the interaction between hydrolyzed APTES molecules and surface silanol groups, resulting in local changes in crystallite environment and preferred orientation. However, the retention of all major sepiolite reflections demonstrates that the fibrous channel-type structure of sepiolite remains intact after functionalization. Therefore, the XRD results confirm that APTES modification occurs primarily through surface grafting while preserving the intrinsic crystalline structure of sepiolite.

3.1.3. TG analysis

Thermogravimetric curves of pristine sepiolite and APTES–functionalized sepiolite are presented in Fig. 4. The thermograms reveal that both samples exhibit four distinct mass–loss stages, characteristic of dehydration and dehydroxylation processes in fibrous sepiolite. Sepiolite contains several types of water associated with different structural environments, including physically adsorbed (hygroscopic) water, zeolitic water located within channel cavities, coordinated water bound to octahedral edge sites, and structural hydroxyl groups within the octahedral sheet. These water species are progressively removed with increasing temperature, consistent with reported dehydration pathways in the literature [25]. The first mass–loss stage (25–200 °C) corresponds to the removal of hygroscopic and zeolitic water. In this temperature range, pristine and modified sepiolite exhibit mass losses of 11.2% and 8.3%, respectively, with T_{max1} values of 74 °C and 93 °C (Table 1.). The reduced mass loss and the shift of T_{max1} toward higher temperature after modification suggest a change in the interaction between surface water molecules and the modified surface. The second stage (250–350 °C) is associated with the release of magnesium–coordinated water molecules bound to the octahedral structure. The T_{max2} values for pristine and modified sepiolite are 284 °C and 362 °C, accompanied by mass losses of 3.3% and 3.0%, respectively. The noticeable increase in T_{max2} after modification suggests that coordinated water is removed at higher temperatures, indicating modification–induced changes in the local bonding environment. The third mass–loss stage (450–600 °C) corresponds to the removal of more strongly bound water species and partial thermal decomposition of grafted organosilane groups. In this region, T_{max3} values of 539 °C (pristine) and 547 °C (modified) were observed. While pristine sepiolite exhibits a mass loss of 2.5%, modified sepiolite shows a significantly higher loss of 11.4%. This pronounced difference is attributed to the thermal decomposition of grafted organosilane chains and confirms that surface modification directly alters the thermal behavior of sepiolite [26,27]. The fourth thermal event, centered near 800 °C, corresponds to dehydroxylation of structural hydroxyl groups. At this stage, pristine and modified sepiolites exhibit mass losses of 3.0% and 2.8%, with T_{max4} values of 809 °C and 787 °C, respectively. The absence of significant additional mass loss

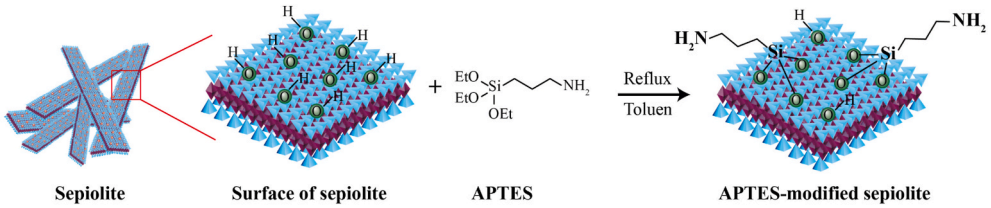

Fig. 2. Proposed silanization mechanism of sepiolite via condensation between surface Si–OH groups and hydrolyzed APTES molecules.

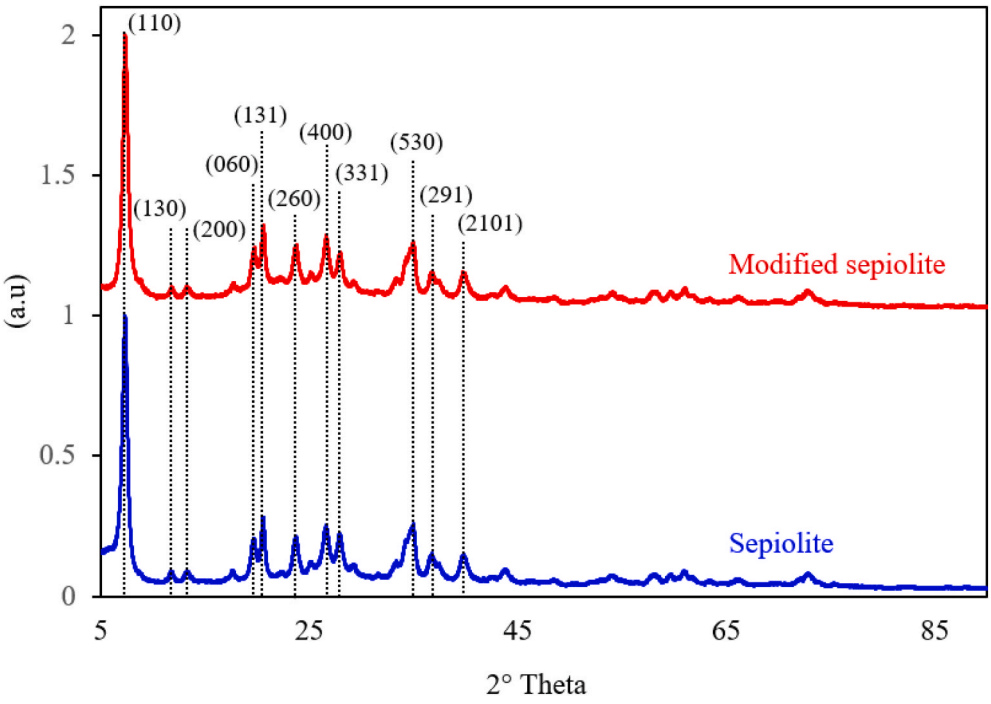

Fig. 3. XRD patterns of pristine sepiolite and APTES-functionalized sepiolite.

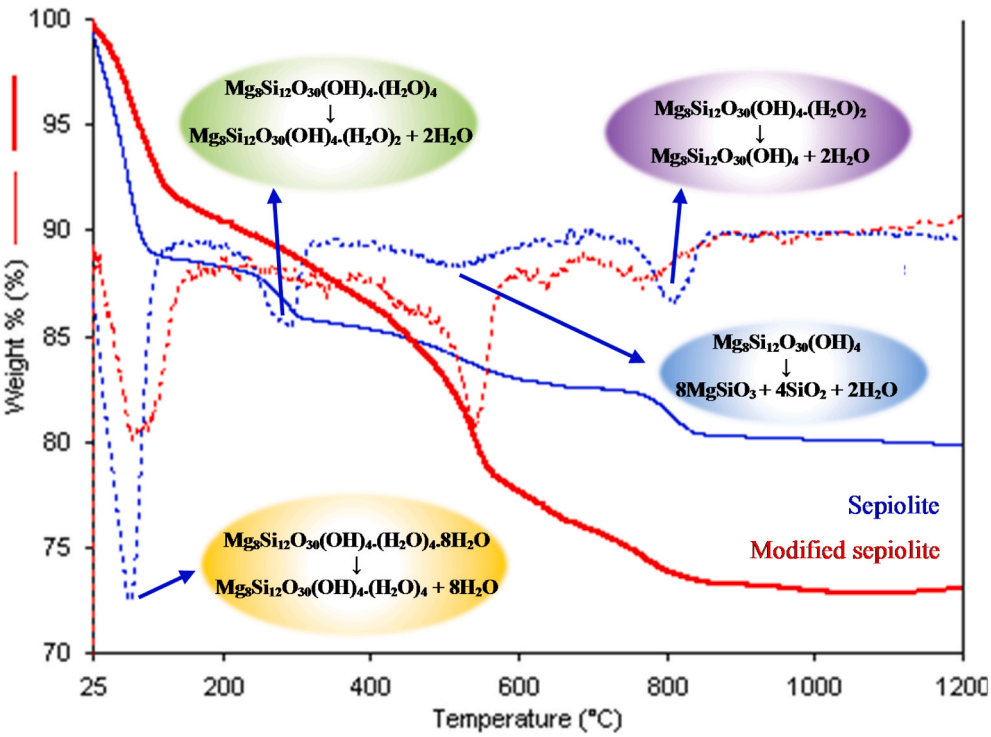

Fig. 4. Thermogravimetric and differential thermal analysis curves of sepiolite and APTES–functionalized sepiolites.

up to 1200 °C suggests that no further major decomposition processes occur at higher temperatures. At 1200 °C, the residual mass is 79.8% for pristine sepiolite and 74.1% for modified sepiolite. The shifts in T_{max} values, redistribution of mass–loss steps, and differences in residual mass collectively provide strong evidence of successful surface modification, indicating that the grafting process alters the thermal response without significantly affecting the structural integrity of the mineral framework. Overall, the upward shift in dehydration temperatures together with modification–dependent changes in mass–loss distribution suggests that silane grafting modifies the bonding environment of water and hydroxyl species, thereby altering thermal stability and providing further evidence of chemical interaction between the modifier and the sepiolite surface.

3.1.4. SEM/EDX analysis

High-resolution FESEM micrographs of pristine sepiolite,

APTES–functionalized sepiolite, and MB–adsorbed modified sepiolite at identical magnifications are presented in Fig. 5. The pristine sepiolite sample (Fig. 5a) exhibits the characteristic needle-like fibrous morphology of natural sepiolite, with individual fibers assembled into bundle-like aggregates. At high magnification, elongated fibers with nanometric diameters and lengths extending to several hundred nanometers can be clearly distinguished, confirming the typical fibrous architecture of sepiolite reported in the literature [28]. The fibers are arranged in interconnected networks, generating accessible inter-fiber voids and channels that are beneficial for adsorption processes. Following APTES functionalization (Fig. 5b), the characteristic fibrous morphology remains largely preserved, indicating that surface modification occurs without significant disruption of the sepiolite framework. Individual fibers remain clearly distinguishable, while localized surface deposits and increased inter-fiber connections can be observed. These features are consistent with the formation of a surface-bound organosilane layer and suggest successful grafting of APTES onto the fiber surfaces. Similar observations have been reported for silane-modified clay minerals [29]. The morphology of the MB-adsorbed APTES-functionalized sepiolite (Fig. 5c) shows a more compact structure compared with the pristine and modified samples. In addition to the preserved fibrous framework, irregular flake-like and aggregated surface features

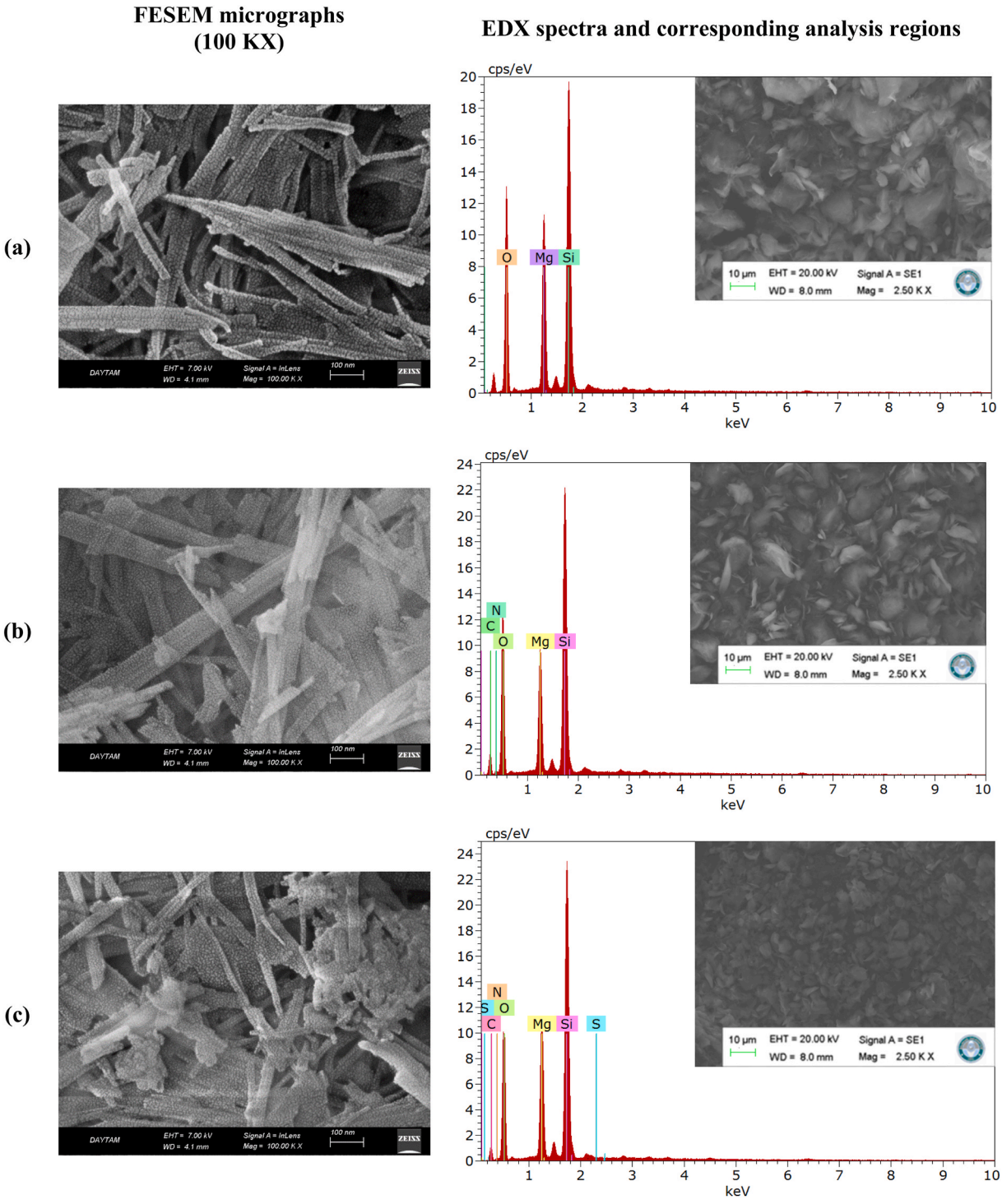

Fig. 5. FESEM micrographs and corresponding EDX spectra of (a) sepiolite, (b) APTES–functionalized sepiolite and (c) MB–adsorbed modified sepiolite.

are observed, indicating the accumulation of adsorbed dye species on the modified surface. The increased aggregation and partial surface coverage observed after adsorption may be associated with interactions between methylene blue molecules and the amine-functionalized sepiolite surface. The progressive morphological evolution from pristine sepiolite to the modified and dye-loaded forms provides visual evidence of surface functionalization and subsequent adsorption.

The elemental compositions of pristine sepiolite, APTES–functionalized sepiolite, and MB–adsorbed modified sepiolite were determined by EDX analysis, and the results are summarized in Table 2. Pristine sepiolite consists primarily of O (51.48 wt%), Si (29.90 wt%), and Mg (18.62 wt%), which is consistent with the typical chemical composition of natural sepiolite. After APTES modification, significant changes in elemental composition were observed. The appearance of carbon (16.65 wt%) and nitrogen (2.97 wt%), which are absent in pristine sepiolite, provides direct elemental evidence for successful grafting of amine-containing functional groups onto the sepiolite surface. Concurrently, the relative contents of Si and Mg decrease to 21.85 wt% and 10.89 wt%, respectively. This reduction is attributed to surface coverage by the organosilane layer, which attenuates the detectable signal of the inorganic substrate. It should be noted that EDX data represent normalized relative elemental percentages. Therefore, slight variations in individual elemental contents, particularly Mg, should be interpreted as changes in the relative elemental distribution within the analyzed region rather than as real changes in the absolute elemental content. This is particularly important when comparing samples with different surface coverages. Following MB adsorption, the elemental distribution changes further. The carbon and nitrogen contents were determined to be 12.48 wt% and 2.09 wt%, respectively. Notably, the emergence of sulfur (0.07 wt%), originating from the sulfonated structure of MB, directly confirms the presence of dye molecules on the adsorbent surface. The absence of sulfur in pristine and solely modified samples further verifies that dye adsorption has occurred. The systematic appearance of C and N after modification and the detection of S after dye adsorption provide strong elemental evidence for successful surface functionalization followed by dye binding. When considered together with the FTIR findings, the observed elemental variations provide complementary evidence for the successful chemical modification of sepiolite and the subsequent adsorption of MB.

Table 2
Elemental composition (wt%) of sepiolite samples.

Samples	Elements (wt%)					
	O	Si	Mg	C	N	S
Sepiolite	51.48	29.90	18.62	–	–	–
APTES–functionalized sepiolite	47.64	21.85	10.89	16.65	2.97	–
MB–adsorbed modified sepiolite	46.26	24.67	13.10	12.48	2.09	0.07

3.1.5. BET surface area and pore structure analysis

The nitrogen adsorption–desorption isotherms and pore size distribution curves (Fig. 6) clearly reveal that pristine sepiolite possesses a hierarchical micro–mesoporous structure. The textural parameters derived from the adsorption–desorption isotherms are summarized in Table 3. The steep adsorption uptake at low relative pressure observed in Fig. 6a indicates dominant micropore filling, while the pronounced hysteresis loop at intermediate and high relative pressures reflects capillary condensation within mesopores. According to IUPAC (2015), this behavior corresponds to a combined Type I(b)–Type IV(a) isotherm with H3–type hysteresis. This adsorption signature is fully consistent with the fibrous morphology and intrinsic channel–type pore architecture of sepiolite reported in previous studies [30,31]. The high BET surface area (244 m^2/g) and significant micropore volume (0.193 cc/g) quantitatively support this structural interpretation. A clear transformation in adsorption behavior is observed after amino–silane functionalization. As shown in Fig. 6b, the micropore uptake in the low–pressure region nearly disappears and the total adsorbed volume decreases significantly, indicating blockage of micropores and a shift toward mesopore–controlled adsorption. The reduction in BET surface area from 244 to 109 m^2/g and the apparent loss of microporosity strongly suggest that grafted organosilane molecules partially obstruct internal channels and reduce pore accessibility. Similar pore blocking effects following surface functionalization have been widely reported for modified clay minerals [24,32].

After MB adsorption, a further decrease in adsorption volume is observed (Fig. 6c). The cumulative pore volume curves presented in Fig. 6d show a pronounced reduction across the entire pore radius range, demonstrating that dye molecules occupy not only external surfaces but also internal pore structures. The weakening of peaks in the dV(log r) distribution suggests that dye molecules occupy a substantial fraction of the available pore volume rather than being restricted solely to the external surface. Interestingly, despite the substantial reduction in BET surface area and total pore volume after modification, an increase in MB adsorption capacity is observed. This apparent contradiction demonstrates that adsorption performance is governed primarily by surface chemistry rather than textural properties. The grafted amine functionalities introduce specific adsorption that strongly interact with cationic dye molecules through electrostatic attraction, hydrogen bonding, and possible surface complexation. Similar behavior has been reported for functionalized clay minerals, where adsorption efficiency is more strongly influenced by surface chemistry than by textural characteristics [33,34]. These results highlight a fundamental shift in the structure–function relationship induced by functionalization. In pristine sepiolite, adsorption behavior is primarily governed by the micro–mesoporous architecture, whereas in modified sepiolite, surface functional groups dominate and the adsorption mechanism becomes chemically controlled. Therefore, after functionalization, the chemical nature and density of active surface sites become the dominant factor governing adsorption performance, rather than purely textural limitations.

3.2. Electrokinetic properties

Zeta potential measurements provide valuable insight into the modification-induced changes in the electrokinetic behavior of sepiolite. The isoelectric point (IEP) of natural sepiolite has previously been reported to be approximately pH 6.6, where the surface is positively charged below this value and negatively charged above it [35]. In this study, the zeta potential of APTES–functionalized sepiolite was evaluated over the pH range of 2–11, and the results are presented in Fig. 7. The modified sepiolite exhibits an isoelectric point at pH 3.54, indicating a pronounced shift toward more acidic values compared to pristine sepiolite. This shift is likely associated with the condensation reaction between surface silanol (Si–OH) groups and the organosilane modifier, which reduces the density of ionizable hydroxyl groups and alters the surface chemical environment. The zeta potential profile

Table 1
Thermal stability parameters of sepiolite and modified sepiolite.

Samples	T_{max1} (°C)	$DeltaY_1$ (wt%)	T_{max2} (°C)	$DeltaY_2$ (wt%)	T_{max3} (°C)	$DeltaY_3$ (wt%)	T_{max4} (°C)	$DeltaY_4$ (wt%)	Residue (wt%)
Sepiolite	74	11.2	284	3.3	539	2.5	809	3.0	79.8
APTES–functionalized sepiolite	93	8.3	362	3.0	547	11.4	787	2.8	74.1

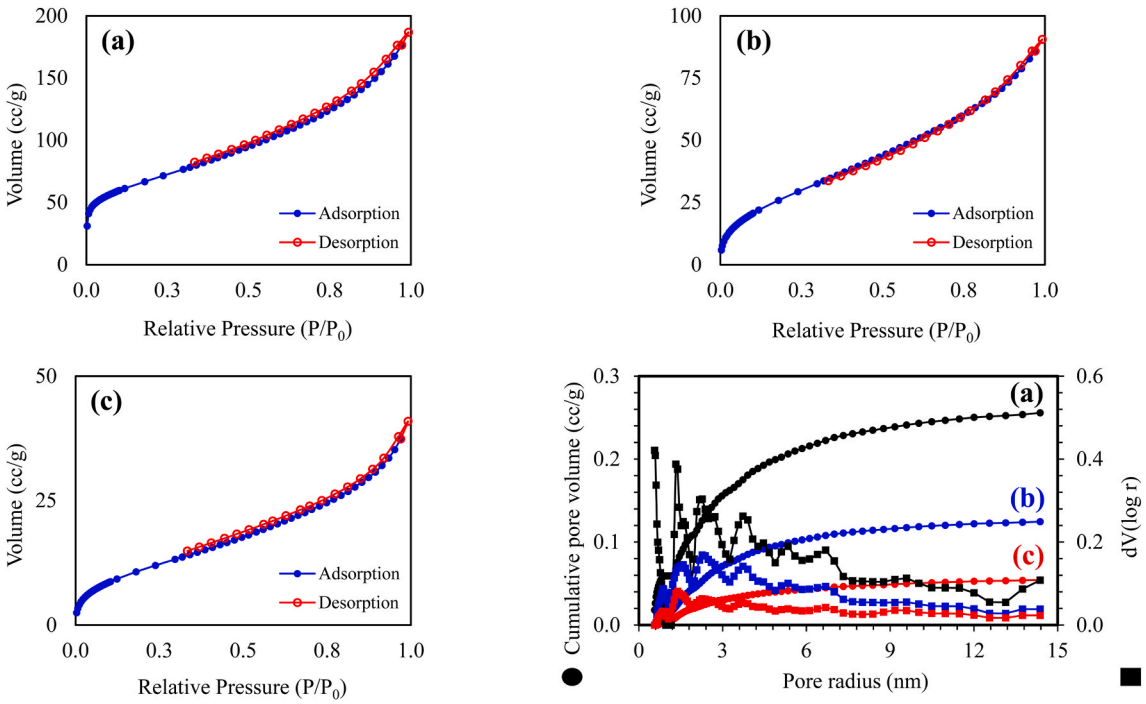

Fig. 6. Nitrogen adsorption–desorption isotherms of (a) sepiolite, (b) APTES–functionalized sepiolite (c) MB–adsorbed modified sepiolite and (d) Cumulative pore volume and dV(log r) distributions of sepiolite samples.

Table 3
BET surface area and pore volume distribution (micro–, meso–, and macropores) of sepiolite samples.

Samples	S_{BET} (m^2/g)	Total pore volume (cc/g)	DFT pore volume (cc/g)	Micro pore volume (cc/g)	Meso pore volume (cc/g)	Macro pore volume (cc/g)
Sepiolite	244	0.289	0.256	0.193	0.063	0.033
APTES–functionazed sepiolite	109	0.140	0.126	0	0.126	0.014
MB–adsorbed modified sepiolite	44	0.063	0.055	0	0.055	0.008

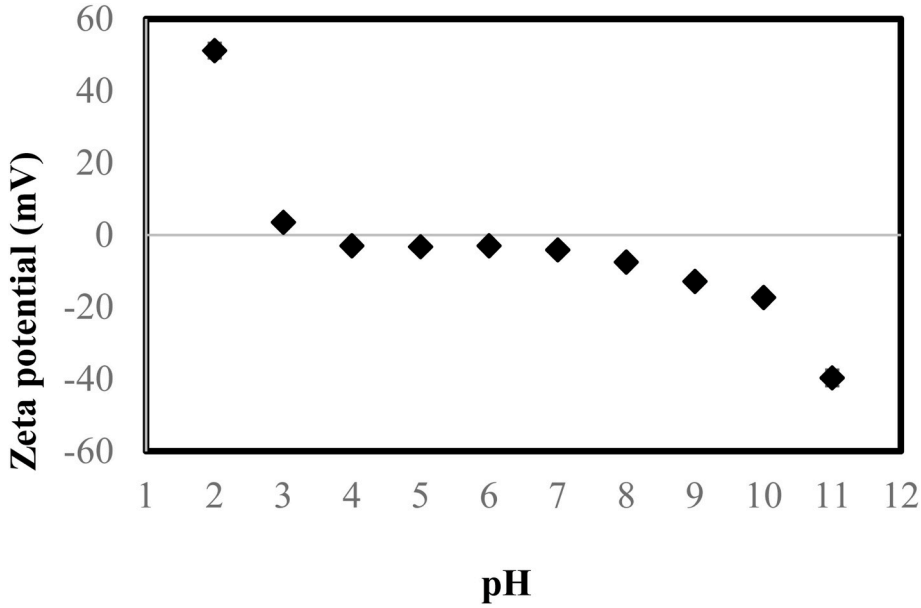

Fig. 7. The variation of zeta potential to pH of APTES–functionalized sepiolite suspensions.

clearly shows that the modified sepiolite surface is positively charged below pH 3.54 and negatively charged above this value. The pH–dependent surface charging behavior and the corresponding protonation/deprotonation reactions are schematically illustrated in Fig. 8.

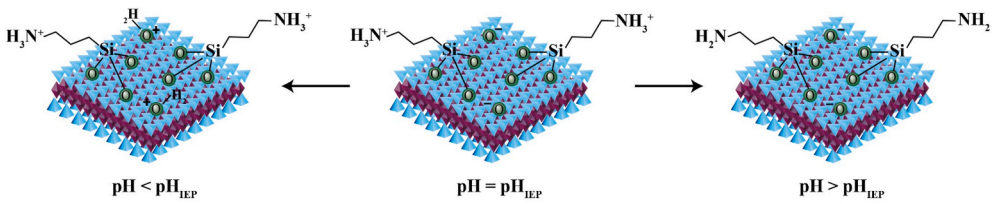

Fig. 8. Change in surface charge of APTES–functionalized sepiolite at the isoelectric point (pH_{iep}), below it ($pH < pH_{iep}$), and above it ($pH_{iep} < pH$).

Under acidic conditions, protonation of surface silanol and amine groups generates a positively charged surface, whereas at higher pH values, deprotonation leads to the development of negative surface charge. The downward shift of the isoelectric point together with the predominance of negative surface charge over a wide pH range provides further electrokinetic evidence of successful surface functionalization. These findings demonstrate that modification alters the ionization behavior of surface functional groups and redefines the charge distribution at the solid–liquid interface. Overall, the observed shift in zeta potential and the pH–dependent surface charging behavior, consistent with the mechanism illustrated in Fig. 8, confirm that organosilane functionalization significantly modifies the electrokinetic properties of sepiolite.

3.3. Adsorption kinetics of MB on modified sepiolite

For the effective design and scale-up of adsorption systems, it is essential to elucidate the adsorption rate, kinetic behavior, and underlying adsorption mechanism. In this context, the adsorption rate and kinetic behavior of MB on amino–functionalized sepiolite were systematically investigated by considering the effects of stirring speed, initial dye concentration, solution pH, and temperature, and the obtained findings are discussed below.

3.3.1. Effect of stirring speed

The effect of stirring speed on MB adsorption by amino-functionalized sepiolite was investigated at an initial dye concentration of 1×10^{-4} mol/L, 30 °C, and natural pH. The results are presented in Fig. 9a. Experiments were conducted at 250, 500, and 750 rpm. A systematic increase in both adsorption rate and equilibrium uptake was observed with increasing stirring speed. When the stirring speed was increased from 250 rpm to 750 rpm, the adsorbed amount of MB increased from 7.95×10^{-5} mol/g to 9.51×10^{-5} mol/g. This enhancement is attributed to the thinning of the external boundary layer surrounding the adsorbent particles, which increases the external mass transfer coefficient [36,37]. Higher agitation intensifies turbulence in the solution, facilitating the transport of dye molecules from the bulk solution to the adsorbent surface and thereby minimizing film diffusion resistance. The results indicate that at lower stirring speeds, the adsorption process is partially controlled by external film diffusion, whereas increasing agitation reduces this diffusion limitation and accelerates adsorption kinetics. Similar effects of agitation rate on adsorption kinetics have been reported for Cu(II) adsorption onto potato peel biomass [37]. Accordingly, to minimize external mass transfer limitations and ensure kinetically controlled adsorption conditions, subsequent adsorption experiments were performed at a stirring speed of 750 rpm.

3.3.2. Effect of initial dye concentration

The initial dye concentration represents a key driving force governing mass transfer between the aqueous phase and the adsorbent surface, thereby directly influencing adsorption kinetics. The effect of initial MB concentration on the adsorption behavior of modified sepiolite was investigated at 750 rpm and 30 °C, and the results are presented in Fig. 9b. The adsorption system approached equilibrium within approximately 5 h, with slight variations depending on the initial MB concentration. An increase in the initial dye concentration led to a pronounced increase in the equilibrium adsorption capacity (q_e). Specifically, the equilibrium adsorption amount increased from

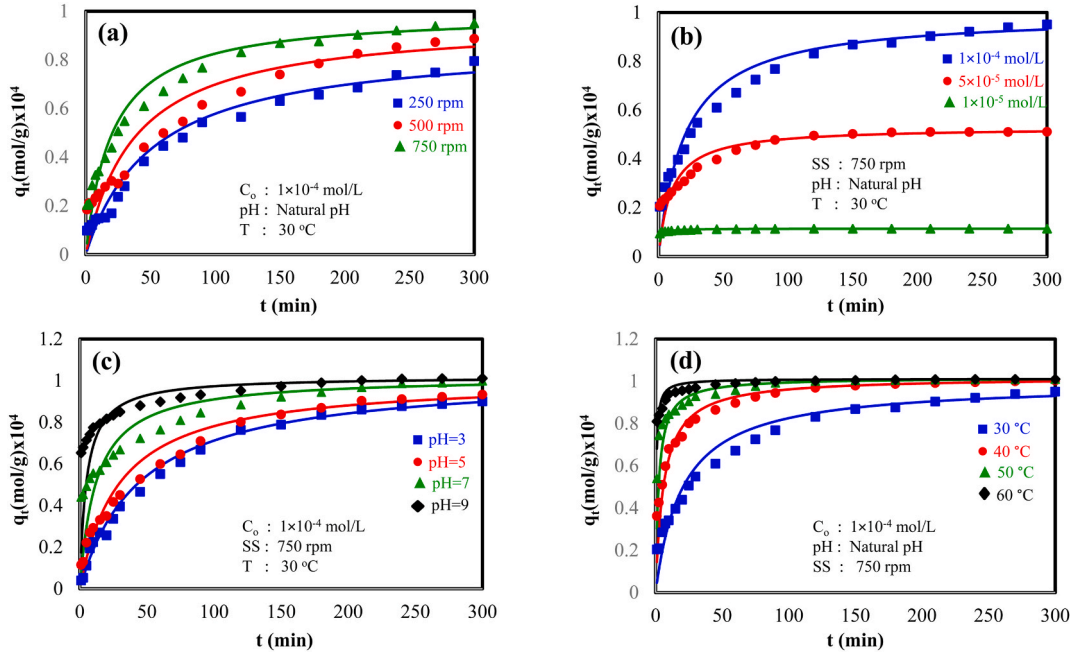

Fig. 9. The effect of (a) stirring speed, (b) initial dye concentration, (c) pH and (d) temperature on the adsorption rate of MB on APTES–functionalized sepiolite.

1.14×10^{-5} mol/g to 9.51×10^{-5} mol/g when the initial concentration was raised from 1×10^{-5} mol/L to 1×10^{-4} mol/L. This trend can be attributed to the increased concentration gradient between the bulk solution and the adsorbent surface at higher initial concentrations, which increases the mass transfer driving force. The stronger concentration gradient accelerates solute transport toward available active sites, particularly during the early adsorption stage. Similar concentration–dependent behavior has been reported for dye adsorption systems in previous studies [37,38]. Although the adsorption capacity per unit mass increased with concentration, a relative decrease in removal efficiency was observed at higher initial concentrations. This behavior is associated with faster saturation of accessible active sites and the limited number of adsorption centers available on the modified sepiolite surface. Overall, the results demonstrate that the adsorption capacity and kinetic behavior of MB on modified sepiolite are strongly concentration–dependent and controlled by the concentration–gradient–driven mass transfer process. These findings are consistent with previous literature reports [37,38] and further confirm the important role of the initial solute concentration in governing adsorption performance.

3.3.3. Effect of pH

Solution pH is a critical parameter governing adsorption kinetics and capacity by controlling surface charge distribution and the ionization state of functional groups. The effect of initial solution pH to MB adsorption onto modified sepiolite was investigated at $C_0 = 1 \times 10^{-4}$ mol/L, 750 rpm, and 30 °C, and the results are presented in Fig. 9c. The results clearly demonstrate that both adsorption rate and equilibrium uptake increase systematically with increasing pH. When the initial pH increased from 3 to 9, the adsorbed amount of MB increased from 8.99×10^{-5} mol/g to 1.01×10^{-4} mol/g. This behavior is directly associated with the electrokinetic properties of the modified sepiolite surface. Zeta potential measurements revealed that the isoelectric point (pH_{IEP}) of modified sepiolite is pH 3.54 (Fig. 7). Accordingly, the surface is positively charged at pH < 3.54 and negatively charged at pH > 3.54. At low pH values, protonation of surface amine ($–NH_2$) and silanol groups results in a positively charged surface, leading to electrostatic repulsion with cationic MB molecules. In addition, competition between H^+ ions and dye molecules for active adsorption sites further suppresses adsorption. As pH increases, deprotonation of surface functional groups occurs, generating a negatively charged surface that enhances electrostatic attraction between the adsorbent and cationic MB molecules. This enhanced electrostatic attraction promotes both adsorption rate and equilibrium adsorption capacity. Therefore, the adsorption behavior is strongly governed by the pH–dependent surface charge characteristics of the modified sepiolite. Similar pH–dependent enhancement in MB adsorption has been reported for sepiolite, perlite, and raw apricot kernel shell adsorbents [17,39,40]. Overall, the findings demonstrate that MB adsorption onto modified sepiolite is highly pH–sensitive and predominantly controlled by electrostatic interactions arising from pH–dependent surface charge variations. These results are fully consistent with the electrokinetic analysis and further confirm that surface functionalization modulates adsorption performance through charge–controlled adsorption mechanisms.

3.3.4. Effect of temperature

Temperature is a key parameter that directly influences both adsorption kinetics and equilibrium capacity, providing important insight into the thermodynamic nature of the adsorption process. The effect of temperature on MB adsorption onto modified sepiolite was investigated at natural pH and a stirring speed of 750 rpm, and the results are presented in Fig. 9d. The results clearly show that both the adsorption rate and equilibrium uptake increase with increasing temperature. When the temperature was raised from 30 °C to 60 °C, the amount of adsorbed MB increased from 9.51×10^{-5} mol/g to 1.01×10^{-4} mol/g. Increasing temperature enhances the mobility of dye molecules and reduces solution viscosity, thereby decreasing mass transfer resistance between the liquid phase and the adsorbent surface. This promotes faster transport of MB molecules toward active adsorption sites, particularly during the initial stage of adsorption. In addition, elevated temperature improves intraparticle diffusion by facilitating the penetration of dye molecules into internal pore structures, increasing accessibility to active sites. As reported by Doğan et al. (2007), temperature variations can significantly influence the equilibrium adsorption capacity of an adsorbent for a given adsorbate [41]. The observed increase in equilibrium adsorption capacity with temperature suggests that the adsorption process is endothermic in nature. This endothermic behavior suggests that higher temperatures facilitate overcoming the energy barrier associated with adsorption and enhance adsorbent–adsorbate interactions. Overall, the results demonstrate that increasing temperature promotes MB adsorption onto modified sepiolite from both kinetic and thermodynamic perspectives, further supporting the endothermic nature of the adsorption process.

3.4. Kinetic modeling of MB adsorption

Kinetic modeling provides valuable insight into adsorption rates, reaction order, and the underlying adsorption mechanism, all of which are critical for evaluating process efficiency and scale-up potential. In this study, the kinetic behavior of MB adsorption onto modified sepiolite was analyzed using the pseudo–first–order and pseudo–second–order kinetic models. The pseudo–first–order model is expressed as:

$$\ln(q_e - q_t) = \ln q_e - k_1 t \tag{2}$$

where q_e (mol/g) is the equilibrium adsorption capacity, q_t (mol/g) is the amount adsorbed at time t, and k_1 (1/min) is the pseudo–first–order rate constant. The pseudo–second–order model is given by:

$$\frac{t}{q_t} = \frac{1}{k_2 q_e^2} + \frac{t}{q_e} \tag{3}$$

where k_2 (g/mol min) is the pseudo–second–order rate constant. The values of k_2 and q_e were obtained from the slope and intercept of the t/q_t versus t plot. Application of both kinetic models to the experimental data obtained under different stirring speeds, initial dye concentrations, pH values, and temperatures yielded the regression coefficients (R^2), rate constants, and calculated equilibrium adsorption capacities summarized in Table 4. The pseudo–first–order model produced R^2 values in the range of 0.914–0.995, whereas the pseudo–second–order model showed superior agreement with R^2 values between 0.965 and 0.999. Moreover, the equilibrium adsorption capacities calculated from the pseudo–second–order model ($q_{e,cal}$) were in closer agreement with the experimental values ($q_{e,exp}$) compared to those obtained from the pseudo–first–order model. The fitted kinetic curves generated using the pseudo–second–order parameters exhibited excellent agreement with experimental data over the entire adsorption period (Fig. 9). These results demonstrate that the adsorption kinetics are more accurately described by the pseudo–second–order model, indicating that the adsorption rate is better described by the pseudo-second-order kinetic model and is strongly influenced by surface-related interactions (see Table 5).

Similar kinetic behavior has been reported for the biosorption of Remazol Black B onto *Rhizopus arrhizus* [42], adsorption of Congo red and 2–chlorophenol onto coir pith–derived activated carbon [43,44], and the adsorption of MB and related dyes onto perlite [17,45].

To quantitatively evaluate adsorption rate, the half–life ($t^{1/2}$) values were calculated using:

$$t_{1/2} = \frac{1}{k_2 q_e} \tag{4}$$

The calculated half–life values (Table 4) decrease with increasing stirring speed, pH, and temperature, whereas they increase with increasing initial dye concentration, confirming that enhanced mass

Table 4
Kinetic constants for MB adsorption on APTES–functionazed sepiolite.

Parameters				Kinetics models								$t_{1/2}$ (min)
C_o (mol/L)	pH	T (°C)	Stirring speed (rpm)	Pseudo–first–order model				Pseudo–second–order model				
				R^2	k_1 (g/mol min)	$q_{e(cal)}$ (mol/g)× 10^5	$q_{e(exp)}$ (mol/g)× 10^5	k_2 (g/mol min)	R^2	$q_{e(cal)}$ (mol/g)× 10^5	$q_{e(exp)}$ (mol/g)× 10^5	
1×10^{-4}	Natural pH	30	250	0.989	0.010	6.995	7.949	221.36	0.965	8.768	7.949	56.83
1×10^{-4}	Natural pH	30	500	0.974	0.012	7.917	8.867	276.82	0.972	9.613	8.867	40.74
1×10^{-4}	Natural pH	30	750	0.987	0.014	6.808	9.506	495.51	0.995	9.934	9.506	21.23
5×10^{-5}	Natural pH	30	750	0.987	0.026	3.215	5.108	1911.39	0.999	5.298	5.108	10.24
1×10^{-5}	Natural pH	30	750	0.914	0.018	0.083	1.142	107207.31	0.999	1.144	1.142	0.82
1×10^{-4}	3.0	30	750	0.995	0.015	8.476	8.994	215.24	0.994	10.323	8.994	51.66
1×10^{-4}	5.0	30	750	0.995	0.015	8.029	9.325	337.57	0.991	10.102	9.325	31.77
1×10^{-4}	7.0	30	750	0.989	0.014	5.485	9.989	812.99	0.997	10.198	9.989	12.31
1×10^{-4}	9.0	30	750	0.952	0.019	3.428	10.109	2019.07	0.999	10.203	10.109	4.90
1×10^{-4}	Natural pH	40	750	0.970	0.017	3.876	10.034	1624.04	0.999	10.196	10.034	6.14
1×10^{-4}	Natural pH	50	750	0.981	0.023	2.197	10.096	4187.60	0.999	10.175	10.096	2.36
1×10^{-4}	Natural pH	60	750	0.975	0.022	0.521	10.106	20335.77	0.999	10.120	10.106	0.49

Natural pH refers to the original pH of the suspension without adjustment using HCl or NaOH.

Table 5
Intraparticle diffusion parameters and regression coefficients for MB adsorption on APTES–functionazed sepiolite under different experimental conditions.

Parameters				Mechanism of adsorption					
C_o (mol/L)	pH	T (°C)	Stirring speed (rpm)	Intraparticle diffusion					
				$k_{int,1} \times 10^6$ (mol/g $min^{1/2}$)	R_1^2	$k_{int,2} \times 10^6$ (mol/g $min^{1/2}$)	R_2^2	$k_{int,3} \times 10^6$ (mol/g $min^{1/2}$)	R_3^2
1×10^{-4}	Natural pH	30	250	2.00	0.960	6.65	0.987	3.40	0.985
1×10^{-4}	Natural pH	30	500	3.29	0.969	6.49	0.983	2.92	0.977
1×10^{-4}	Natural pH	30	750	7.56	0.983	5.28	0.997	1.74	0.982
5×10^{-5}	Natural pH	30	750	3.15	0.979	2.84	0.994	0.23	0.764
1×10^{-5}	Natural pH	30	750	0.31	0.885	0.03	0.886	0.01	0.965
1×10^{-4}	3.0	30	750	8.85	0.964	7.47	0.988	2.10	0.936
1×10^{-4}	5.0	30	750	8.26	0.963	6.69	0.995	1.84	0.938
1×10^{-4}	7.0	30	750	5.57	0.971	4.47	0.989	1.54	0.958
1×10^{-4}	9.0	30	750	5.53	0.992	2.22	0.977	0.76	0.881
1×10^{-4}	Natural pH	40	750	14.60	0.987	4.08	0.950	0.52	0.978
1×10^{-4}	Natural pH	50	750	12.81	0.823	2.14	0.954	0.14	0.951
1×10^{-4}	Natural pH	60	750	2.99	0.990	0.46	0.965	0.06	0.886

Natural pH refers to the original pH of the suspension without adjustment using HCl or NaOH.

transfer and surface interaction accelerate the adsorption process. Overall, the kinetic analysis confirms that MB adsorption onto modified sepiolite is best described by the pseudo–second–order model, highlighting the important contribution of surface-related interactions to the overall adsorption kinetics.

Identification of the rate–limiting step is essential for elucidating the overall adsorption mechanism. In general, adsorption proceeds through three sequential stages: *(i)* transport of the adsorbate from the bulk solution to the external surface of the adsorbent (film diffusion), *(ii)* diffusion within the internal pore structure (intraparticle diffusion), and *(iii)* adsorption at active surface sites. Based on the combined kinetic and electrokinetic findings, MB adsorption onto modified sepiolite follows a multi–step mechanism rather than a single rate–controlling process. The intraparticle diffusion behavior was evaluated using the Weber–Morris model:

$$q_t = k_{int}\sqrt{t} + C \tag{5}$$

where q_t is the adsorption amount at time t, k_{int} is the intraparticle diffusion rate constant, and C represents the boundary layer thickness parameter. The non–zero intercept values ($C \neq 0$) indicate that intraparticle diffusion is not the sole rate–limiting step and that external film diffusion contributes to the overall kinetics. As shown in Fig. 10, the q_t versus $t^{1/2}$ plots do not pass through the origin and exhibit multiple linear regions. This multi–linearity clearly demonstrates that the adsorption process occurs in distinct stages, involving successive diffusion and surface interaction steps. The calculated intraparticle diffusion rate constants (k_{i2}) ranged between 0.03×10^{-6} and 7.47×10^{-6} mol/g min. The initial linear portion corresponds to rapid external mass transfer (film diffusion), followed by a second region associated with intraparticle diffusion within the porous structure. The final plateau region reflects equilibrium establishment and surface–site saturation [46]. When evaluated together with the superior fitting of the pseudo–second–order kinetic model, the results suggest that surface-related interactions become increasingly important during the final stage of the adsorption process. The kinetic evidence confirms that adsorption is not governed solely by diffusion but involves strong specific interactions between MB molecules and functionalized surface sites. The dominant interactions in the final adsorption stage include electrostatic attraction between cationic MB molecules and negatively charged surface sites,

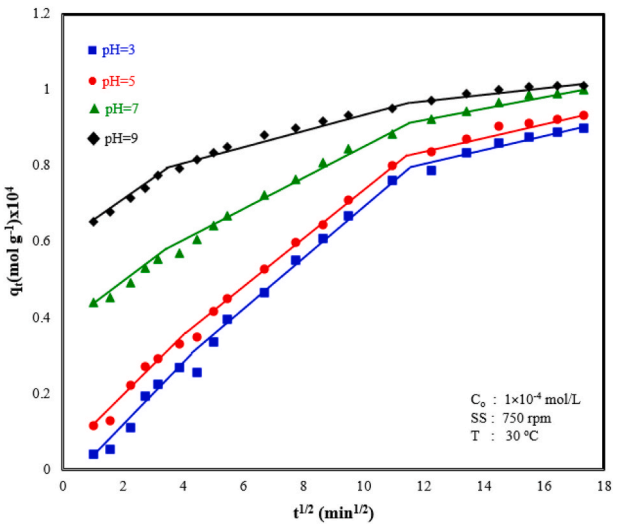

Fig. 10. Intraparticle diffusion plots for different pHs.

hydrogen bonding, and possible surface complexation involving amino–functional groups. Similar adsorption behavior–characterized by pseudo–second–order kinetics combined with multi–step diffusion mechanisms–has been reported for MB adsorption onto various clay–based and nanostructured adsorbents [46]. Overall, the proposed mechanism describes a diffusion–assisted process: MB molecules are first transported through the boundary layer, then diffuse within the pore structure, and finally interact strongly with surface functional groups, which govern the overall adsorption performance.

3.5. Hydrogen storage

The pressure– and temperature–dependent hydrogen storage behavior of pristine sepiolite and APTES–functionalized sepiolite provides valuable insight into the relationship between surface accessibility, pore architecture, and hydrogen adsorption behavior. Examination of the excess hydrogen adsorption isotherms at room and cryogenic temperatures presented in Fig. 11 clearly demonstrates that hydrogen adsorption is not governed solely by pressure. Rather, it is controlled by a multi–parameter equilibrium involving temperature, pore accessibility, and the superposition of adsorption potential fields. The pronounced capacity difference observed between cryogenic and room–temperature conditions strongly confirms that the hydrogen storage mechanism is predominantly governed by physisorption.

According to the numerical data derived from the isotherms in Fig. 11, the hydrogen storage capacity of sepiolite at room temperature is approximately 0.06 wt% at 10 bar, increasing to 0.69 wt% at 104 bar. Under identical conditions, the modified sepiolite exhibits capacities of 0.05 wt% and 0.60 wt%, respectively, clearly indicating that pristine sepiolite maintains superior storage performance across the entire pressure range. At cryogenic temperature, the hydrogen storage capacity of sepiolite increases from 0.81 wt% at 10 bar to 2.53 wt% at 104 bar, whereas the modified sepiolite increases from 0.29 wt% to 1.76 wt%. This comparison clearly reveals that decreasing temperature and increasing pressure significantly enhance hydrogen storage capacity, and that sepiolite consistently outperforms modified sepiolite under all investigated conditions. The higher hydrogen storage capacity of sepiolite at both room and cryogenic temperatures is directly associated with its specific surface area and pore structure. As shown in Table 3, the high surface area and significant micropore volume of sepiolite provide a larger adsorption potential field for hydrogen molecules. In contrast, organosilane functionalization partially blocks micropore entrances and reduces the total surface area, leading to decreased hydrogen adsorption capacity in the modified sample. Alver (2018) emphasized that the fibrous channel–like pore structure of sepiolite facilitates physical hydrogen adsorption, particularly at low temperatures, distinguishing it from other clay minerals. The present results clearly demonstrate that the microporous channel structure of sepiolite enhances hydrogen confinement and thus improves storage capacity [47]. In the study by Bicil (2026), functionalization of MWCNTs resulted in decreased in BET surface area and micropore volume but a substantial increase in mesopore volume, which was accompanied by enhanced hydrogen storage performance [48]. This behavior highlights that hydrogen storage is governed not only by total surface area but also by pore accessibility, pore size distribution, and the balance between micro- and mesoporosity. These findings demonstrate that hydrogen storage performance is governed not solely by total surface area but by the overall balance between micro– and mesoporosity, pore accessibility, and pore architecture. A numerical comparison of temperature effects shows that the hydrogen storage capacity of sepiolite increases from 0.69 wt% at 104 bar and room temperature to 2.53 wt% at the same pressure under cryogenic conditions, corresponding to an approximately 3.7–fold enhancement. For modified sepiolite, the capacity increases from 0.60 wt% to 1.76 wt%, representing an approximately 2.9–fold increase. This difference is attributed to the higher micropore volume of pristine sepiolite, which promotes stronger overlap of adsorption potential fields and enhances hydrogen confinement at cryogenic temperatures.

Wang et al. (2024) reported that palygorskite systems exhibit lower hydrogen storage capacity compared to sepiolite, based on both experimental and simulation studies. Structural analyses indicated that sepiolite possesses higher micropore volume and greater channel continuity, which support enhanced adsorption [12]. The higher experimental hydrogen storage capacity of sepiolite observed in the present study, compared with that reported for palygorskite, further supports the view that micropore accessibility and channel continuity are critical parameters governing hydrogen storage performance. Although both sepiolite and palygorskite display fibrous morphologies, sepiolite contains wider and more continuous three–dimensional channel systems. These channels provide greater effective pore volume and more homogeneous micropore distribution, whereas palygorskite channels are narrower and segmented. From a microstructural perspective, the inter–wall distance

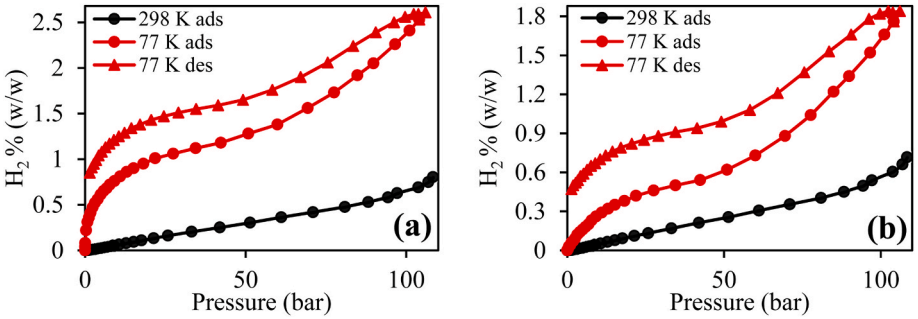

Fig. 11. Pressure-dependent hydrogen adsorption isotherms of (a) sepiolite and (b) APTES–functionalized sepiolite.

in sepiolite channels is more compatible with the kinetic diameter of hydrogen molecules, leading to stronger overlap of adsorption potential fields. In contrast, the narrower and irregular channels of palygorskite partially restrict hydrogen diffusion and reduce adsorption volume. Consequently, adsorption in palygorskite occurs predominantly near surface regions, while volumetric micropore filling is more effective in sepiolite. This structural difference explains the superior cryogenic hydrogen storage capacity of sepiolite. Campos et al. (2008) reported that untreated montmorillonite stores approximately 0.12 wt% hydrogen at 77 K, while silica–intercalated montmorillonite reaches 0.40 wt%, attributed to mesopore development [49]. In comparison, the intrinsic channel structure of sepiolite provides inherent pore accessibility advantages similar to artificially expanded structures in layered clays. Therefore, sepiolite exhibits more efficient micropore filling and higher hydrogen storage capacity than many layered clay minerals reported in the literature.

At cryogenic temperature, the observed capacity enhancement for both samples is associated with reduced kinetic energy of hydrogen molecules, allowing longer residence time within the adsorption potential field. Particularly in narrow and accessible micropores, the overlap of adsorption potentials significantly enhances hydrogen confinement. Wang et al. (2023) similarly reported that hydrogen adsorption in microporous silicate and clay–based adsorbents increases substantially at low temperatures, controlled by micropore filling mechanisms [10]. The cryogenic adsorption isotherm behavior observed for sepiolite in the present study further supports a micropore–controlled physisorption mechanism. The cryogenic isotherms of sepiolite exhibit a steep initial slope at low pressure, characteristic of dominant micropore filling. In contrast, modified sepiolite shows a lower initial slope and limited capacity. At room temperature, both samples exhibit significantly reduced hydrogen storage capacities compared to cryogenic conditions due to the weakening of physisorption interactions at elevated temperature. With respect to pressure effects, increasing pressure from 10 to 104 bar at room temperature increases the capacity of sepiolite from 0.06 wt% to 0.69 wt% (approximately 11–fold), and from 0.81 wt% to 2.53 wt% (approximately 3–fold) at cryogenic temperature. For modified sepiolite, the corresponding increases are from 0.05 wt% to 0.60 wt% (approximately 12–fold) at room temperature and from 0.29 wt% to 1.76 wt% (approximately 6–fold) at cryogenic temperature. These numerical trends clearly demonstrate that pressure elevation increases hydrogen density, allowing more molecules to be accommodated within the adsorption potential field. Moreover, hydrogen adsorption increases linearly with pressure in accordance with Henry's law. Another reason why the storage capacity of sepiolite samples increases with increasing pressure is that the increased density of hydrogen leads to greater interaction with the surface [8]. The fact that sepiolite shows a more significant increase in capacity at cryogenic temperatures suggests that micropores play a dominant role in hydrogen adsorption. Karadaş et al. (2026) reported strong correlations between hydrogen storage capacity and textural properties of porous carbons, with correlation coefficients of 0.87 for BET surface area and 0.86 for micropore volume. These findings support that hydrogen adsorption is strongly governed by surface area and micropore development. The present results similarly demonstrate that hydrogen storage capacity in sepiolite is directly related to its specific surface area and micropore volume. In modified sepiolite, the reduction of surface area and elimination of microporosity limit hydrogen storage performance, confirming that pore accessibility and micropore density dominate over chemical functionalization in determining hydrogen storage behavior [50].

A comparison of the hydrogen storage capacities of clay minerals reported in the literature with the sepiolite and modified sepiolite results obtained in this study is presented in Table 6. Literature data indicate that hydrogen storage capacity depends strongly not only on material type but also on measurement conditions, particularly temperature and pressure. Near room temperature, Wang et al. (2023) reported a hydrogen storage capacity of 1.37 wt% for sepiolite at 273 K and 180 bar [10], while Zhang et al. (2024) reported 0.12 wt% at 273 K and 100 bar [13]. In the present study, sepiolite exhibits 0.69 wt% at 298 K and 104 bar. Although measured at lower pressure than in Wang et al. (2023), this value exceeds that reported by Zhang et al. (2024), highlighting the importance of pore accessibility and micropore architecture. Under the same conditions (298 K, 104 bar), modified sepiolite exhibits 0.60 wt% hydrogen storage. The decrease relative to pristine sepiolite is attributed to reduced micropore accessibility and specific surface area following functionalization.

Table 6
Comparison of hydrogen storage capacities of clay minerals under different pressure and temperature conditions based on the literature.

Samples	Pressure (bar)	Temperature (K)	wt% H_2	References
Playgorskite	180	273	1.06	[10]
Sepiolite	180	273	1.37	[10]
Playgorskite	180	338	0.036	[12]
Sepiolite	180	338	0.134	[12]
Montmorillonite	70	77	0.11	[11]
Montmorillonite	70	195	0.10	[11]
Montmorillonite	70	303	0.04	[11]
Na–Montmorillonite	90	363	0.20	[9]
Montmorillonite	100	273	0.012	[13]
Sepiolite	100	273	0.12	[13]
Laponite	80	77	0.5–1	[51]
Sepiolite	104	77	2.53	In this study
Sepiolite	104	298	0.69	In this study
APTES–functionalized sepiolite	104	77	1.76	In this study
APTES–functionalized sepiolite	104	298	0.60	In this study

Comparisons performed under cryogenic temperature conditions more clearly reveal the pronounced superiority of sepiolite over other clay minerals. Wolff-Boenisch et al. (2023) reported a hydrogen storage capacity of approximately 0.11 wt% for montmorillonite at 77 K and 70 bar [1]. Similarly, Edge (2015) reported a capacity in the range of 0.5–1 wt% for laponite at 77 K and 80 bar [51]. In contrast, in the present study, the sepiolite sample reached a hydrogen storage capacity of approximately 2.53 wt% at 77 K and 104 bar. This value is several times higher than those of layered clay minerals and indicates that the fibrous channel–type pore architecture of sepiolite significantly enhances micropore filling at cryogenic temperature. The modified sepiolite sample exhibited a capacity of 1.76 wt% under the same cryogenic conditions, lower than pristine sepiolite but still markedly higher than the values reported for montmorillonite and laponite. These results clearly demonstrate that changes in pore architecture directly influence hydrogen storage performance.

A comparison between sepiolite and fibrous clay minerals such as palygorskite further highlights the decisive role of pore architecture in hydrogen storage behavior. Wang et al. (2023) reported hydrogen storage capacities of approximately 1.06 wt% for palygorskite and 1.37 wt% for sepiolite at 273 K and 180 bar [10]. In a subsequent study conducted at higher temperature, Wang et al. (2024) reported capacities of approximately 0.036 wt% for palygorskite and 0.134 wt% for sepiolite at 338 K and 180 bar [12]. These results indicate that, although both minerals exhibit fibrous morphology, sepiolite consistently provides higher storage capacity. When compared with layered clay minerals, the advantages of sepiolite becomes even more evident. In layered minerals such as montmorillonite, kaolinite, and illite, hydrogen adsorption is primarily governed by surface adsorption and limited interlayer spacing, whereas the three–dimensional channel system of sepiolite allows hydrogen molecules to be access and occupy the internal pore volume. This structural advantage, particularly under cryogenic conditions where micropore filling becomes dominant, substantially enhances storage capacity. Compared with the low hydrogen storage capacities

reported for montmorillonite, the significantly higher capacity of sepiolite further supports the critical role of fibrous channel–type pore architecture in the hydrogen storage mechanism.

Overall, literature data demonstrate that hydrogen storage performance in sepiolite is sensitive to temperature and pressure, while pore architecture remains the primary structural factor governing storage behavior. In particular, micropore accessibility, channel continuity, and the three–dimensional pore network enable sepiolite to exhibit higher hydrogen storage capacity than both layered clay minerals and structurally similar fibrous clay materials. The results obtained for modified sepiolite further demonstrate that alterations in pore architecture directly influence storage capacity and clearly confirm the critical role of micropore accessibility and pore density in hydrogen adsorption.

3.6. Kinetic modelling of hydrogen storage

The time–dependent hydrogen adsorption data obtained at cryogenic temperature are presented in Fig. 12. The curves recorded for both sepiolite samples clearly exhibit the typical two–stage kinetic behavior commonly observed in gas–solid adsorption systems: an initial rapid adsorption stage followed by a slower approach to equilibrium. The sharp increase in the amount of adsorbed hydrogen during the first minute is associated with the initially vacant active sites on the surface and the high probability of interaction of hydrogen molecules with these sites. As time progresses, the number of available sites decreases and the system gradually approaches equilibrium, resulting in a marked reduction in adsorption rate and the formation of a plateau region. Such a kinetic profile is well known for gas–phase adsorption systems and has been widely reported in the literature [52].

When the effect of pressure is considered, the results obtained at fixed pressures of 35, 50, and 70 bar under cryogenic conditions show that both the initial adsorption rate and the equilibrium capacity increase systematically with increasing pressure (Fig. 12). For pristine sepiolite, the hydrogen uptake after approximately 4 min reaches ~0.55 mmol g^{-1} at 35 bar, ~1.09 mmol g^{-1} at 50 bar, and ~1.69 mmol g^{-1} at 70 bar. For modified sepiolite, the corresponding values at the same time are ~0.55, ~1.15, and ~1.59 mmol g^{-1}, respectively. This trend clearly indicates that increasing pressure raises the number of hydrogen molecules interacting with the adsorbent surface, leading to faster surface filling and higher equilibrium capacity. A similar pressure–dependent enhancement in adsorption kinetics has also been reported for various porous adsorbent systems [50].

Consistent with the isotherm results, pristine sepiolite exhibits a higher maximum adsorption capacity than modified sepiolite under cryogenic conditions (Fig. 11). This suggests that the pore architecture of pristine sepiolite provides a more favorable environment for hydrogen storage. Although surface modification alters the chemical characteristics of the material, it does not completely eliminate the intrinsic advantage of the natural structure in terms of adsorption capacity. Previous studies have also emphasized that changes in surface chemistry and pore structure directly influence both adsorption capacity and kinetic behavior [53].

The formation of a plateau within approximately 2–3 min indicates that the system reaches equilibrium in a relatively short time. Such rapid equilibration behavior is frequently analyzed using pseudo–first–order and particularly pseudo–second–order kinetic models, which often yield high correlation coefficients [8]. However, the observed change in slope of the curves suggests that more than one transport or rate–controlling step may be involved in the adsorption process.

The kinetic analysis of the time–dependent hydrogen adsorption data obtained at cryogenic temperature was performed using the pseudo–first–order and pseudo–second–order models described in Section 3.4. For both sepiolite samples, the linear fit of the pseudo–second–order kinetic model is clearly observed in the t/q_t–t plots presented in Fig. 13, and the high R^2 values together with the strong agreement between $q_{e\,(exp)}$ and $q_{e(cal)}$ reported in Table 7 confirm that the second–order kinetic approach successfully represents the experimental data. First, when the regression coefficients are examined, the R^2 values for the pseudo–first–order model for pristine sepiolite were determined as 0.7235, 0.6909, and 0.5977 at 70, 50, and 35 bar, respectively. In contrast, for the pseudo–second–order model, the R^2 values at the same pressures were significantly higher, reaching 0.9978, 0.9976, and 0.9912. A similar trend was observed for modified sepiolite. While the R^2 values for the pseudo–first–order model ranged between 0.6369 and 0.7525, those for the pseudo–second–order model were in the range of 0.9938–0.9960, indicating an excellent fit. These results clearly demonstrate that, even solely based on regression coefficients, the second–order model provides a much better agreement with the experimental data. Secondly, when the equilibrium adsorption capacities are compared, the $q_{e(cal)}$ values calculated from the pseudo–second–order model show very close agreement with the experimental $q_{e(exp)}$ values. For instance, for pristine sepiolite at 70 bar, $q_{e(exp)}$ was 1.756 mmol/g, while $q_{e(cal)}$ was calculated as 1.747 mmol/g. Similarly, at 50 bar, the values were 1.180 and 1.169 mmol/g, and at 35 bar, 0.637 and 0.580 mmol/g, respectively. For modified sepiolite, comparable agreement was obtained, with values of 1.681–1.636 mmol/g at 70 bar, 1.266–1.227 mmol/g at 50 bar, and 0.599–0.579 mmol/g at 35 bar. This close correspondence indicates that the pseudo–second–order model is not only superior in terms of linear regression but also more reliable in predicting physically meaningful equilibrium parameters. Examination of the rate constant (k_2) values shows that k_2 increases as pressure decreases for both materials (e.g., for pristine sepiolite, from 3.93 at 70 bar to 11.12 at 35 bar). This suggests that although the equilibrium capacity is lower at reduced pressure, the system exhibits a relatively faster kinetic approach per unit of adsorbed hydrogen at the initial stage. Similar pressure–dependent kinetic behavior has been reported for porous carbon–based adsorbents [8,53]. In the literature, hydrogen adsorption kinetics are frequently reported to be better described by the pseudo–second–order model. In particular, studies conducted on microporous carbons have demonstrated high R^2 values and strong q_e agreement in favor of the second–order model [8,52,53]. The findings of the present study are consistent with these reports. In conclusion, considering the regression coefficients, the agreement between $q_{e(exp)}$ and $q_{e(cal)}$, and the overall parameter consistency, it is clearly demonstrated that

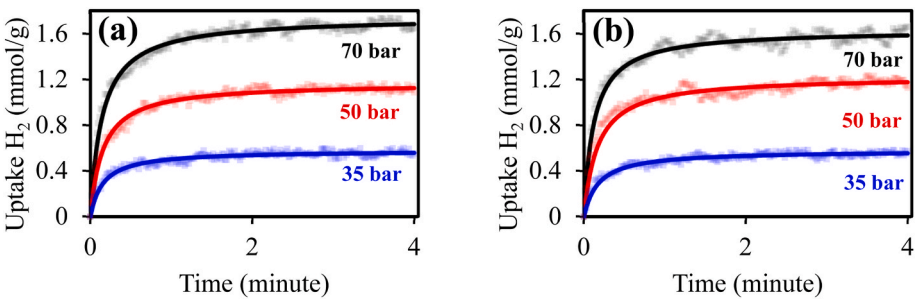

Fig. 12. Time–dependent kinetic behavior of hydrogen adsorption in (a) sepiolite and (b) APTES–functionalized sepiolite at different constant pressures.

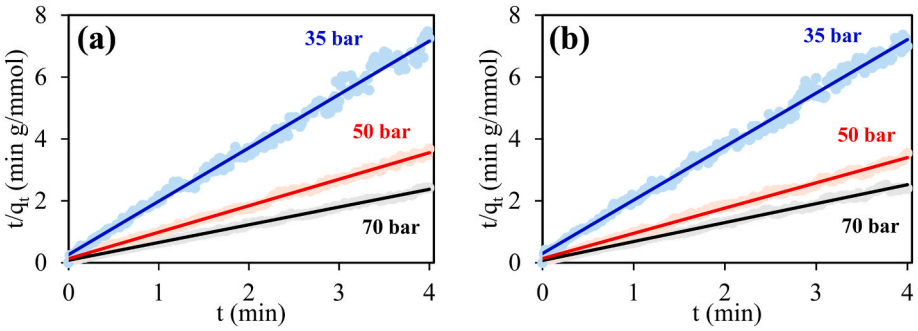

Fig. 13. Pressure–dependent pseudo–second–order kinetic plots (t/q_t vs. t) for hydrogen adsorption on (a) sepiolite and (b) APTES–functionalized sepiolite.

Table 7
Comparative kinetic modelling of hydrogen adsorption on sepiolite and APTES–functionalized sepiolite.

Samples	Pressure (bar)	First order R^2	Second order				Weber-Morris			
			R^2	$q_{e(exp)}$ (mmol/g)	$q_{e(cal)}$ (mmol/g)	k_2 (mmol/g min)	R_1^2	k_1 (mol/g $min^{1/2}$)	R_2^2	k_2 (mol/g $min^{1/2}$)
Sepiolite	70	0.7235	0.9978	1.756	1.747	3.93	0.9752	2.582	0.7574	0.296
	50	0.6909	0.9976	1.180	1.169	5.52	0.9748	1.591	0.7138	0.209
	35	0.5977	0.9912	0.637	0.580	11.12	0.9705	0.803	0.6697	0.101
APTES–functionazed sepiolite	70	0.6369	0.9960	1.681	1.636	5.01	0.9821	2.645	0.6863	0.219
	50	0.7525	0.9959	1.266	1.227	4.84	0.9791	1.840	0.7917	0.186
	35	0.6468	0.9938	0.599	0.579	9.76	0.9644	0.861	0.7124	0.108

hydrogen adsorption on both pristine and modified sepiolite at cryogenic temperature follows the pseudo–second–order kinetic model more closely than the pseudo–first–order model.

The time–dependent hydrogen adsorption data obtained at cryogenic temperature were analyzed using the Weber–Morris intraparticle diffusion model described in Section 3.4, and the results revealed a two–stage linear behavior (Table 7, Fig. 14). The presence of two distinct linear slopes in the q_t–$t^{1/2}$ plots indicates that the adsorption process is not governed by a single rate–limiting step, but rather involves successive mass transfer and diffusion stages. This behavior is consistent with the multi–step kinetic nature commonly reported for gas–phase adsorption on porous solid adsorbents [8,52]. For pristine sepiolite, the regression coefficients corresponding to the first linear region (R_1^2) were determined as 0.9705, 0.9748, and 0.9752 at 35, 50, and 70 bar, respectively. Similarly, the R_1^2 values for modified sepiolite ranged between 0.9644 and 0.9821 (Table 7). These high correlation coefficients indicate that the model describes the initial stage of adsorption very well. The slope values (k_1) of the first region increase significantly with increasing pressure. For example, for pristine sepiolite, the k_1 value rises from 0.803 at 35 bar to 2.582 at 70 bar, while for modified sepiolite it increases from 0.861 to 2.645 (Table 7). This increase reflects the acceleration of the initial mass transfer process due to the higher hydrogen density at elevated pressure. Similar pressure–dependent increases in the intraparticle diffusion coefficient have been reported for carbon nanotubes and other microporous adsorbents [48,50]. In contrast, the R_2^2 values corresponding to the second linear region are noticeably lower than those of the first region (0.6697–0.7574 for pristine sepiolite and 0.6863–0.7917 for modified sepiolite) (Table 7). This suggests that the second stage is governed by a more complex diffusion regime, during which the adsorption rate gradually decreases as the system approaches equilibrium. The k_2 values are also considerably lower than k_1, further supporting this interpretation. For instance, for pristine sepiolite at 70 bar, $k_1 = 2.582$ while $k_2 = 0.296$ (Table 7). This pronounced difference implies that the first stage is associated with rapid surface filling or external film diffusion, whereas the second stage is controlled by intraparticle diffusion within the pore structure and a gradual approach to equilibrium.

The fact that the linear plots do not pass through the origin in the graphs (Fig. 13) also indicates that intraparticle diffusion is not the sole rate–limiting step. If the process were controlled exclusively by pore diffusion, the linear lines would be expected to intersect the origin. However, the observed intercepts demonstrate that an initial boundary layer (film) resistance also contributes to the overall adsorption process. A similar multi–stage transport mechanism has previously been reported for carbon–based adsorbents [7,8]. When pristine and modified sepiolite are compared, the two–stage kinetic behavior is preserved for both samples; however, the higher k_1 values observed for pristine sepiolite, particularly at elevated pressure, indicate a more favorable initial

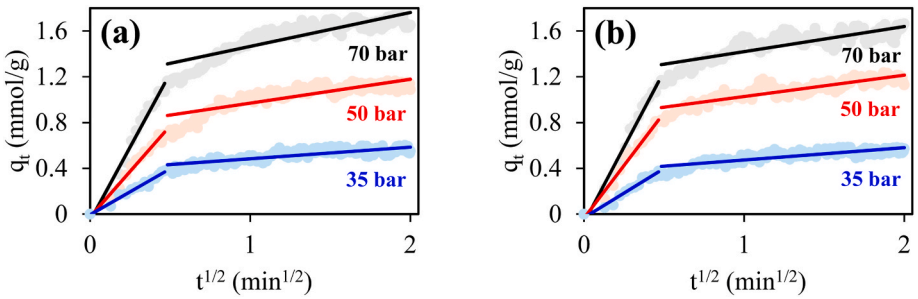

Fig. 14. Weber–Morris intraparticle diffusion plots for hydrogen adsorption on (a) sepiolite and (b) APTES–functionalized sepiolite.

adsorption rate. This behavior can be attributed to the more accessible microporous structure of natural sepiolite. In contrast, the similar diffusion rates observed for both materials during the second stage suggest that intraparticle transport becomes the dominant factor as the system approaches equilibrium. Overall, the Weber–Morris analysis reveals that hydrogen adsorption under cryogenic conditions follows a two–step kinetic mechanism, involving an initial rapid surface/external film transfer followed by a slower intraparticle diffusion stage. When considered together with the pseudo–second–order kinetic analysis, these findings strongly support that the system exhibits a multi–stage transport behavior governed primarily by physical adsorption.

4. Conclusions

In this study, the adsorption behaviors of natural sepiolite and APTES–functionalized sepiolite in both liquid and gas phases were systematically and comparatively investigated, and the structure–surface–function relationship governing adsorption performance was comprehensively elucidated. Characterization results demonstrated that surface functionalization preserves the intrinsic fibrous channel architecture of sepiolite while reducing micropore accessibility and BET surface area. Despite this reduction, the enhanced MB adsorption capacity observed in the liquid phase clearly indicates that adsorption performance depends not solely by textural properties but predominantly by surface chemistry and the density of active functional groups. Electrokinetic analysis provided direct mechanistic evidence supporting this behavior. The pronounced shift of the isoelectric point toward acidic pH values after APTES functionalization and the predominance of negative surface charge over a wide pH range confirmed that surface protonation–deprotonation reactions strongly regulate adsorbent–adsorbate interactions. This electrokinetic modification enhances electrostatic attraction between negatively charged surface sites and cationic MB molecules, thereby promoting adsorption capacity and rate. Kinetic modeling revealed that the adsorption process is best described by the pseudo–second–order model, indicating the important contribution of surface-related interactions to the adsorption process. Weber–Morris analysis further demonstrated a multi–step diffusion mechanism involving initial film diffusion followed by intraparticle diffusion and surface interaction processes. Together with the electrokinetic findings, these results confirm that liquid-phase adsorption is primarily governed by surface charge–controlled interaction mechanisms rather than purely textural effects. Hydrogen storage measurements in the gas phase showed that adsorption is primarily controlled by physisorption and strongly influenced by temperature, pressure, and particularly micropore structure. Natural sepiolite exhibited consistently higher hydrogen storage capacity than the modified sample under all investigated conditions, owing to its higher micropore volume and superior channel continuity. The pronounced capacity enhancement observed under cryogenic conditions confirms that micropore filling and the overlap of adsorption potential fields play a decisive role in the hydrogen storage mechanism. Comparison with literature data further indicates that the three–dimensional channel architecture of sepiolite provides superior hydrogen storage performance compared to layered clay minerals. Overall, while electrokinetically controlled surface chemistry dominates adsorption in the liquid phase, pore architecture governs adsorption behavior in the gas phase. This work establishes a robust scientific basis for the design of multifunctional clay-based adsorbents capable of integrating environmental pollutant removal and hydrogen storage within a single material platform.

Ethical approval

No experiments were conducted in this study that required ethical approval.

Funding

This work was supported by the Scientific Research Projects Commission of Balikesir University (Project Number: BAP 2021/106).

Declaration of competing interest

The authors declare the following financial interests/personal relationships which may be considered as potential competing interests: This work was supported by Balikesir University (Project Number: BAP 2021/106).

Data availability

Data will be made available on request.

References

[1] H. Xue, X. Wang, Q. Xu, F. Dhaouadi, L. Sellaoui, M.K. Seliem, A.B. Lamine, H. Belmabrouk, A. Bajahzar, A. Bonilla-Petriciolet, Z. Li, Q. Li, Adsorption of methylene blue from aqueous solution on activated carbons and composite prepared from an agricultural waste biomass: a comparative study by experimental and advanced modeling analysis, Chem. Eng. J. 430 (2022) 132801, https://doi.org/10.1016/j.cej.2021.132801.

[2] A. Thakur, H. Kaur, Response surface optimization of Rhodamine B dye removal using paper industry waste as adsorbent, Int. J. Ind. Chem. 8 (2017) 175–186, https://doi.org/10.1007/s40090-017-0113-4.

[3] Z. Cheng, R. Yang, X. Zhu, Adsorption behaviors of the methylene blue dye onto modified sepiolite from its aqueous solutions, Desalination Water Treat. 57 (2016) 25207–25215, https://doi.org/10.1080/19443994.2016.1144535.

[4] K. Sharma, S. Sharma, V. Sharma, P.K. Mishra, A. Ekielski, V. Sharma, V. Kumar, Methylene blue dye adsorption from wastewater using hydroxyapatite/gold nanocomposite: kinetic and thermodynamics studies, Nanomaterials 11 (2021) 1403, https://doi.org/10.3390/nano11061403.

[5] T. Perraki, A. Orfanoudaki, Study of raw and thermally treated sepiolite from the Mantoudi area, Euboea, Greece: X-ray diffraction, TG/DTG/DTA and FTIR investigations, J. Therm. Anal. Calorim. 91 (2008) 589–593, https://doi.org/10.1007/s10973-007-8329-8.

[6] M. Mora, M.Á. Carmona, C. Jiménez-Sanchidrián, M.I. López, J.R. Ruiz, Sepiolite as environmental friendly and reusable catalyst for the selective synthesis of (E)-nitrostyrenes, React. Kinet. Mech. Catal. 99 (2010) 303–309, https://doi.org/10.1007/s11144-010-0150-x.

[7] M. Doğan, M.Y. Kalafat, B.K. Kızılduman, Z. Bicil, Y. Turhan, E. Yanmaz, B. Duman, Hydrogen storage analysis of fullerene and defective fullerenes: the first experimental study, Fuel 390 (2025) 134705, https://doi.org/10.1016/j.fuel.2025.134705.

[8] Y. Turhan, B. Duman, M. Doğan, E. Yanmaz, Z. Bicil, B.K. Kızılduman, Enhanced hydrogen storage in lithium-doped defective fullerenes: experimental optimization, adsorption mechanisms, and kinetic–isotherm modeling, Diam. Relat. Mater. (2026) 113399, https://doi.org/10.1016/j.diamond.2026.113399.

[9] C. Mondelli, F. Bardelli, J.G. Vitillo, M. Didier, J. Brendle, D.R. Cavicchia, J. C. Robinet, L. Charlet, Hydrogen adsorption and diffusion in synthetic Na-montmorillonites at high pressures and temperature, Int. J. Hydrogen Energy 40 (2015) 2698–2709, https://doi.org/10.1016/j.ijhydene.2014.12.038.

[10] L. Wang, J. Cheng, Z. Jin, Q. Sun, R. Zou, Q. Meng, K. Liu, Y. Su, Q. Zhang, High-pressure hydrogen adsorption in clay minerals: insights on natural hydrogen exploration, Fuel 344 (2023) 127919, https://doi.org/10.1016/j.fuel.2023.127919.

[11] D. Wolff-Boenisch, H.R. Abid, J.E. Tucek, A. Keshavarz, S. Iglauer, Importance of clay–H_2 interactions for large-scale underground hydrogen storage, Int. J. Hydrogen Energy 48 (2023) 13934–13942, https://doi.org/10.1016/j.ijhydene.2022.12.324.

[12] L. Wang, Z. Jin, J. Cheng, Q. Sun, K. Liu, Q. Zhang, Are palygorskite and sepiolite the potential materials for underground hydrogen storage? J. Energy Storage 81 (2024) 110397 https://doi.org/10.1016/j.est.2023.110397.

[13] Q. Zhang, M. Masoudi, L. Sun, L. Zhang, L. Yang, Y. Song, A. Hassanpouryouzband, Hydrogen and cushion gas adsorption–desorption dynamics on clay minerals, ACS Appl. Mater. Interfaces 16 (2024) 53994–54006, https://doi.org/10.1021/acsami.4c12931.

[14] C.K. Back, G. Sandí, J. Prakash, J. Hranisavljevic, Hydrogen sorption on palladium-doped sepiolite-derived carbon nanofibers, J. Phys. Chem. B 110 (2006) 16225–16231, https://doi.org/10.1021/jp061925p.

[15] M. Doğan, Y. Turhan, M. Alkan, H. Namlı, P. Turan, Ö. Demirbaş, Functionalized sepiolite for heavy metal ions adsorption, Desalination 230 (2008) 248–268, https://doi.org/10.1016/j.desal.2007.11.029.

[16] Ö. Demirbaş, M. Alkan, M. Doğan, Y. Turhan, H. Namlı, P. Turan, Electrokinetic and adsorption properties of sepiolite modified by 3-aminopropyltriethoxysilane, J. Hazard. Mater. 149 (2007) 650–656, https://doi.org/10.1016/j.jhazmat.2007.04.036.

[17] M. Doğan, M. Alkan, A. Türkyilmaz, Y. Özdemir, Kinetics and mechanism of removal of methylene blue by adsorption onto perlite, J. Hazard. Mater. 109 (2004) 141–148, https://doi.org/10.1016/j.jhazmat.2004.03.003.
[18] E.E. Doğan, P. Tokcan, B.K. Kızılduman, Storage of hydrogen in activated carbons and carbon nanotubes, Adv. Mater. Sci. 18 (2018) 5–16, https://doi.org/10.1515/adms-2017-0045.
[19] M. Doğan, M. Alkan, Ü. Çakir, Electrokinetic properties of perlite, J. Colloid Interface Sci. 192 (1997) 114–118, https://doi.org/10.1006/jcis.1997.4913.
[20] A. Tabak, E. Eren, B. Afsin, B. Caglar, Determination of adsorptive properties of a Turkish sepiolite for removal of Reactive Blue 15 anionic dye from aqueous solutions, J. Hazard. Mater. 161 (2009) 1087–1094, https://doi.org/10.1016/j.jhazmat.2008.04.062.
[21] B.M. Smith, S.E. Lappi, S.H. Brewer, S. Dembowy, J. Belyea, S. Franzen, Covalent attachment of a nickel nitrilotriacetic acid group to a germanium attenuated total reflectance element, Langmuir 20 (2004) 1184–1188, https://doi.org/10.1021/la034194i.
[22] L. Li, J. Shi, In situ reduction and nitrification method for the synthesis of Ga and GaN quantum dots in the channels of mesoporous silicon materials, Nanotechnology 17 (2005) 344–348, https://doi.org/10.1088/0957-4484/17/1/059.
[23] R.L. Frost, O.B. Locos, H. Ruan, J.T. Kloprogge, Near-infrared and mid-infrared spectroscopic study of sepiolites and palygorskites, Vib. Spectrosc. 27 (2001) 1–13, https://doi.org/10.1016/S0924-2031(01)00110-2.
[24] O. Turhan, B.K. Kızılduman, Y. Turhan, M. Doğan, Adsorption of methylene blue on imine modified sepiolite from aqueous solutions, Fresenius Environ. Bull. 30 (2021) 196–209.
[25] G. Tartaglione, D. Tabuani, G. Camino, Thermal and morphological characterisation of organically modified sepiolite, Microporous Mesoporous Mater. 107 (2008) 161–168, https://doi.org/10.1016/j.micromeso.2007.04.020.
[26] J. Lemić, M. Tomašević-Čanović, M. Djuričić, T. Stanić, Surface modification of sepiolite with quaternary amines, J. Colloid Interface Sci. 292 (2005) 11–19, https://doi.org/10.1016/j.jcis.2005.05.080.
[27] E. Grządka, E. Godek, T.A. Le, U. Maciołek, M. Galaburda, J. Orzeł, T. Leskinen, T. P. Huynh, Synthesis, properties and applications of new hybrid material based on native/magnetically modified sepiolite and chitosans, Sep. Purif. Technol. 348 (2024) 127671, https://doi.org/10.1016/j.seppur.2024.127671.
[28] Y. Li, M. Wang, D. Sun, Y. Li, T. Wu, Effective removal of emulsified oil from oily wastewater using surfactant-modified sepiolite, Appl. Clay Sci. 157 (2018) 227–236, https://doi.org/10.1016/j.clay.2018.02.014.
[29] F. Largo, R. Haounati, H. Ouachtak, N. Hafid, A. Jada, A.A. Addi, Design of organically modified sepiolite and its use as adsorbent for hazardous Malachite Green dye removal from water, Water Air Soil Pollut. 234 (2023) 183, https://doi.org/10.1007/s11270-023-06185-z.
[30] F. Franco, M. Pozo, J.A. Cecilia, M. Benítez-Guerrero, E. Pozo, J.A. Martín Rubí, Microwave assisted acid treatment of sepiolite: the role of composition and “crystallinity”, Appl. Clay Sci. 102 (2014) 15–27, https://doi.org/10.1016/j.clay.2014.10.013.
[31] L. González Hernández, L. Ibarra Rueda, A. Rodríguez Díaz, C. Chamorro Antón, Preparation of amorphous silica by acid dissolution of sepiolite: kinetic and textural study, J. Colloid Interface Sci. 109 (1986) 150–160, https://doi.org/10.1016/0021-9797(86)90290-0.
[32] M.A. Moreira, K.J. Ciuffi, V. Rives, M.A. Vicente, R. Trujillano, A. Gil, E.H. de Faria, Effect of chemical modification of palygorskite and sepiolite by 3-aminopropyl-triethoxisilane on adsorption of cationic and anionic dyes, Appl. Clay Sci. 135 (2017) 394–404, https://doi.org/10.1016/j.clay.2016.10.022.
[33] K. Song, G. Sandí, Characterization of montmorillonite surfaces after modification by organosilane, Clays Clay Miner. 49 (2001) 119–125, https://doi.org/10.1346/CCMN.2001.0490202.
[34] E.H. Meftah, O.S. Salhah, H.F. Wahıda, Modification of kaolinite clay using benzyltriethylammonium chloride as a surfactant: preparation and characterization, Int. J. Eng. Technol. 9 (2020) 850, https://doi.org/10.14419/IJET.V9I4.31088.
[35] M. Doğan, H. Abak, M. Alkan, Adsorption of methylene blue onto hazelnut shell: Kinetics, mechanism and activation parameters, J. Hazard. Mater. 164 (2009) 172–181, https://doi.org/10.1016/j.jhazmat.2008.07.155.
[36] I. Ghodbane, O. Hamdaoui, Removal of mercury(II) from aqueous media using eucalyptus bark: kinetic and equilibrium studies, J. Hazard. Mater. 160 (2008) 301–309, https://doi.org/10.1016/j.jhazmat.2008.02.116.
[37] E.K. Guechi, O. Hamdaoui, Evaluation of potato peel as a novel adsorbent for the removal of Cu(II) from aqueous solutions: equilibrium, kinetic, and thermodynamic studies, Desalination Water Treat. 57 (2015) 10677–10688, https://doi.org/10.1080/19443994.2015.1038739.
[38] M. Alkan, Ö. Demirbaş, M. Doğan, Adsorption kinetics and thermodynamics of an anionic dye onto sepiolite, Microporous Mesoporous Mater. 101 (2007) 388–396, https://doi.org/10.1016/j.micromeso.2006.12.007.
[39] Z.X. Han, Z. Zhu, D.D. Wu, J. Wu, Y.R. Liu, Adsorption kinetics and thermodynamics of Acid Blue 25 and methylene blue dye solutions on natural sepiolite, Synth. React. Inorg., Met.-Org., Nano-Met. Chem. 44 (2013) 140–147, https://doi.org/10.1080/15533174.2013.770755.
[40] O.O. Namal, E. Kalipci, Adsorption kinetics of methylene blue removal from aqueous solutions using potassium hydroxide (KOH) modified apricot kernel shells, Int. J. Environ. Anal. Chem. 100 (2020) 1549–1564, https://doi.org/10.1080/03067319.2019.1656721.
[41] M. Doğan, Y. Özdemir, M. Alkan, Adsorption kinetics and mechanism of cationic methyl violet and methylene blue dyes onto sepiolite, Dyes Pigments 75 (2007) 701–713, https://doi.org/10.1016/j.dyepig.2006.07.023.
[42] Z. Aksu, S. Tezer, Equilibrium and kinetic modelling of biosorption of Remazol Black B by *Rhizopus arrhizus* in a batch system: effect of temperature, Process Biochem. 36 (2000) 431–439, https://doi.org/10.1016/S0032-9592(00)00233-8.
[43] C. Namasivayam, D. Kavitha, Removal of Congo Red from water by adsorption onto activated carbon prepared from coir pith, an agricultural solid waste, Dyes Pigments 54 (2002) 47–58, https://doi.org/10.1016/S0143-7208(02)00025-6.
[44] C. Namasivayam, D. Kavitha, Adsorptive removal of 2-chlorophenol by low-cost coir pith carbon, J. Hazard. Mater. 98 (2003) 257–274, https://doi.org/10.1016/S0304-3894(03)00006-2.
[45] M. Doğan, M. Alkan, Adsorption kinetics of methyl violet onto perlite, Chemosphere 50 (2003) 517–528, https://doi.org/10.1016/S0045-6535(02)00629-X.
[46] O.O. Namal, E. Kalipci, Adsorption kinetics of methylene blue using alkali and microwave-modified apricot stones, Separ. Sci. Technol. (2018) 1–17, https://doi.org/10.1080/01496395.2018.1541469.
[47] B.E. Alver, Hydrogen adsorption on natural and sulphuric acid treated sepiolite and bentonite, Int. J. Hydrogen Energy 43 (2018) 831–838, https://doi.org/10.1016/j.ijhydene.2017.10.159.
[48] Z. Bicil, Adsorption kinetics and mechanism of hydrogen on pristine and functionalized multi-walled carbon nanotubes, Fuel 403 (2026) 136130, https://doi.org/10.1016/j.fuel.2025.136130.
[49] F. Campos, L. de la Torre, M. Román, A. Garcia, A.A. Elguézabal, Montmorillonite clay intercalated with nanoparticles for hydrogen storage, J. Ceram. Process. Res. 9 (2008) 482–485, https://doi.org/10.36410/jcpr.2008.9.5.482.
[50] M. Karadaş, G. Duman, M. Doğan, Y. Turhan, T. Karayıldırım, Hydrogen storage performance of porous carbons from waste cotton: activation strategies, isotherm and kinetic analyses, Fuel 409 (2026) 137820, https://doi.org/10.1016/j.fuel.2025.137820.
[51] J. Edge, Hydrogen Adsorption and Dynamics in Clay Minerals, University College London (UCL), London, 2015. PhD thesis.
[52] Z.S. Doğan, E.E. Doğan, Z. Bicil, B.K. Kızılduman, The effect of Li-doping and doping methods on hydrogen storage capacities of some carbonaceous materials, Fuel 396 (2025) 135280, https://doi.org/10.1016/j.fuel.2025.135280.
[53] Y. Turhan, M.B. Yeşilbiçer, B.K. Kızılduman, M. Doğan, Z. Bicil, Cryogenic hydrogen storage on peanut shell-derived activated carbons: Isotherm, kinetics and mechanism, J. Energy Storage 140 (2025) 118998, https://doi.org/10.1016/j.est.2025.118998.